SOUTHEAST UNIVERSITY

(formerly NANJING INSTITUTE OF TECHNOLOGY)

Ph.D DISSERTATION

STUDENT: JIAN-YU LU

SUPERVISOR: YU WEI

Department of Biomedical Engineering

Abstract

Diffraction tomography was developed in the late 1970s and is a promising way to solve the diffraction problem in tomographic imaging where the dimension of the details of the object to be imaged are comparable to the wavelength of interacting wave. In this paper, further studies of the reconstruction algorithms of the diffraction tomography are performed and the results show that not only the quality of the reconstructed images is improved greatly, but the time for image reconstruction is reduced obviously.

In addition, a new quantitative reflection imaging method which is based on the transmitting/receiving geometry of the commercially available B-scanner is developed from the theoretical foundations of the diffraction tomography. Besides the theoretical analysis of this new quantitative reflection imaging method, a set of experimental system which includes the interface between the B-scanner and computer is built up and images of several practical testing objects are reconstructed using the data obtained from this experimental system. The results show that the images reconstructed by this new quantitative reflection imaging method are more helpful in understanding the internal structures of testing objects than those obtained by the ordinary B-scanner and to some extent, the images are quantitative. Therefore, this new imaging method will be useful in tissue characterization and will enhance the ability of the ordinary B-scanner for diagnosing disease. It has been shown that this new quantitative reflection imaging method is an important progress in acoustical imaging technique and has a good prospect in practical medical imaging.

Finally, at the end of the paper, some problems which are required to be further studied are demonstrated.

April 30, 1988

CONTENTS

I. INTRODUCTION

A novel imaging technique — X-ray computerized tomography (short for XCT) was developed in the early 1970s[1,2]. The inventors of the XCT, G.N. Hounsfield, the electronic engineer of English EMI cooperation and A.M. Cormack, the America physicist, won the Nobel Prize of physiology and medicine in 1979. Encouraged by the successfulness of the XCT, various kinds of CT with different physical emanations are developed. By the nature of the interacting rays used, the CT imaging techniques can be roughly divided into two categories: the CTs with wavy rays, such as, ultrasonic computerized tomography (UCT)[3-27], microwave computerized tomography (MCT)[28-31], etc., and the CTs with non-wavy rays, such as, XCT[32-44], nuclear magnetic resonant computerized tomography (NMR-CT)[45-48], positron emission computerized tomography (PET)[49], single photon emission computerized tomography (SPECT)[50-52], etc. (in fact, the classification above is not absolute, for the non-wavy rays become the wavy rays if its wavelength is comparable to the dimension of the details of the object to be imaged).

In this paper, the CT techniques with the emanation of wavy rays, especially, the UCT in medical application are concerned. The reason is that as compared with microwave, ultrasonic wave can penetrate deeper in biological soft-tissues, for the ultrasonic wave is less heavily attenuated in the biological soft-tissues when it has the same wavelength as the microwave. As compared with the XCT, the UCT has less hazard to human body and can provide higher contrast images of the biological soft-tissues, and moreover, the imaging equipment of the UCT is simpler and less costed.

So far, the images of the UCT is not so good that they can be applicable in clinic[15,16]. A lot of efforts have been done for correcting the ray-bending effects which affect the quality of the images of the UCT[3,20,25], however, the improvement was not distinct, for the diffraction effects of the ultrasonic wave in the biological soft-tissues is remarkable. To solve the diffraction problem of the wavy ray CT, in 1978, a new CT imaging method — diffraction tomography was put forward by R.K. Mueller et al.[53]. For the diffraction tomography takes the diffraction effects of the wavy rays into account, it is a promising way to improve the quality of the images of the UCT.

The theoretical basis of the diffraction tomography is the inverse scattering solution of the wave equation which is obtained by linearizing a group of nonlinear partial differential equations that govern the rules of the wavy rays interacting with the object to be imaged (such linearization is possible because the amplitude of the waves used is usually very small in medical diagnosis). There are two kinds of methods for the inverse scattering solution of the wave equation. One is iterative method[53-60], which exists the mathematical problems of uniqueness, stableness and convergence in the iteration, and is very time-consumed. Although this method is developed constantly, it is still far from been applicable in practice. Another is the diffraction tomography method, i.e., the method for solving the inverse scattering problem analytically under the condition of first-order approximation (weak scattering approximation). For this paper concerns only the ultrasonic imaging of the biological soft-tissues, the first-order approximation can be used, therefore, the diffraction tomography method is chosen for studying.

Since the concept of the diffraction tomography was put forward, many reconstruction algorithms of the diffraction tomography was studied[61-100]. But, it is required that these algorithms are further improved for the

performances of their speed and image quality. Therefore, in the first part of this paper, some of the reconstruction algorithms of the diffraction tomography are studied in detail in order that they will be quicker as well as be better in the quality of the image reconstructions. In the second part of this paper, a new quantitative reflection imaging method is developed, which obtains the quantitative distribution of the acoustical parameter of the biological soft tissues from the transmitting/receiving geometry of the ordinary B-scanner and the theoretical foundation of the diffraction tomography. It is promising that this new imaging method will enhance the ability of tissue characterization of the ordinary B-scanner.

In algorithm studies of the diffraction tomography, the application of cubic spline interpolation to the densifying of the diffracted data is first investigated. In 1982, A.J. Devaney proposed the filtered-backpropagation reconstruction algorithm of the diffraction tomography (short for Devaney's algorithm)[67], which was looked as one of the important advances in physics[70]. Unfortunately, this algorithm is very time consumed. For instance, it requires approximately $O(N^3 \log_2 N)$ complex multiplications for a NxN pixel image reconstructed from NxN diffracted data (N projections and N samples in each projection). In 1983, S.X. Pan et al. put forward zero-padding densifying Fourier-domain interpolation reconstruction algorithm of the diffraction tomography (short for Pan's algorithm)[91], which not only reduced the computational consumption of Devaney's algorithm obviously, but still kept the high quality of the image reconstructions. It requires only approximately $O(N^2 \log_2 N)$ complex multiplications for reconstructing a NxN pixel image from NxN diffracted data. As the zero-padding technique is applied in the densifying of the diffracted data, the Pan's algorithm is still time-consumed. To further speed up the Pan's algorithm, cubic spline densifying fourier-domain interpolation reconstruction algorithm (short for spline algorithm) is developed. With the spline algorithm, images are reconstructed in high speed as well as in high quality.[A1]

There are two modes of diffraction tomography, one is transmission mode and the other is reflection mode. Because the transmission signal usually represents the low-frequency component of the spatial frequency of the object to be imaged and the reflection signal represents the high-frequency component, to gain higher resolution, a new mode of diffraction tomography —— transmission-reflection diffraction tomography (short for TRDCT) is developed by combining above two kinds of diffraction tomography. However, in the computer simulation of the TRDCT, it is discovered that the high-frequency noise is associated with the image reconstruction of the TRDCT. To diminish the high-frequency noise, nonlinear-smoothing image processing technique[37] is adopted for the processing of the images reconstructed by the TRDCT. The results show that the images reconstructed by the TRDCT and then followed by the process using the nonlinear-smoothing image processing technique are of not only higher resolution than the conventional transmission diffraction tomography, but high quality. In addition, to use the Fourier-domain interpolation reconstruction algorithm in the TRDCT, a group of conversion relationships between the curvilinear coordinates and the rectangular coordinates are derived.[A2]

To get the diffraction tomography applied more easily in practice, in 1982, Dr. D. Nahamoo et al. put forward the synthetic aperture diffraction tomography (short for SADCT)[88] which required its transmitting/receiving system to be rotated around the object to be imaged only once and in principle, any type of insonification can be used. Furthermore, an interpolation-free reconstruction algorithm for the SADCT (short for interpolation-free algorithm) was proposed by them[89]. Because there is a space-variant filter in the interpolation-free algorithm, this algorithm is

time-consumed. In this paper, a computational study of the Fourier-domain interpolation reconstruction algorithm of the synthetic aperture diffraction tomography (short for interpolation algorithm) is carried out and a comparison between the interpolation and the interpolation-free algorithm is performed. The results show that the interpolation algorithm is not only faster then the interpolation-free algorithm (such as, the time required for reconstructing a 128x128 pixel image using the interpolation algorithm is only about 13% of that using the interpolation-free algorithm), but is superior in the quality of the reconstructed images when images are evaluated with the image quality criteria of this paper. In addition, in the computer simulation, it is discovered that because an object whose center is not at the origin of the coordinates will has a fast oscillating phase factor contained in its Fourier-domain, the resolution of the Fourier-domain interpolation will be decreased and thus the quality of the reconstructed images will be degraded if the center of the object is not moved back to the origin of the coordinates before the Fourier-domain interpolation. It is also discovered that for the distribution of the points on which the Fourier transform of the object function is known near the boundaries of the Fourier-domain coverage areas of the SADCT is highly uneven, it will be not accurate to interpolate the grid points near the boundaries of the Fourier-domain coverage areas using the points on which the Fourier transform of the object function is known and using the ordinary interpolation scheme. However, the quality of the reconstructed images will be greatly improved if special consideration is taken for the interpolation using these unevenly distributed points.[A3-A5]

By the studies of the reconstruction algorithms above, the speed of the image reconstructions of these algorithms is increased and the quality of the reconstructed images is improved. Moreover, as several datum acquisition geometries of the diffraction tomography are taken into account, these algorithms are more liable to find practical applications.

In addition to the study of the diffraction tomography, a new quantitative reflection imaging method (short for QRI method) is developed. The imaging procedures of the QRI method are as follows: first, the high-frequency component of the one-dimensional object function on the line along which the focused pulsed acoustical wave is propagated is obtained from the received rf (radio frequency) echo signals; then the low-frequency component of the one-dimensional object function is recovered from the high-frequency component using the a priori knowledges that the outlines of the internal structures of the object and the phases of the rf echo signals returned from these outlines are known and using the GP (Gerchberg-Papoulis) frequency extrapolation technique[93]. From the complete spectrum, the one-dimensional object function can be obtained. With the focused ultrasonic beam scanned linearly in the cross-section of the object to be imaged, two-dimensional sound-speed distribution of the object in that cross-section can be reconstructed. In addition to the new imaging method developed and the theoretical analysis of it, the B-scan system is connected to computer and a set of experimental system which includes some interface circuits is built up. By the data obtained from this experimental system, images of several practical objects are reconstructed. The results show that the images reconstructed by the QRI method are more helpful in understanding the internal structures of the testing objects than those obtained by the ordinary B-scanner, and the images reconstructed are quantitative. Therefore, it is promising that the QRI method can be combined with the ordinary B-scanner and will enhance the ability of the ordinary B-scanner for tissue characterization and for diagnosing diseases.

Finally, the theoretical and experimental problems of the diffraction tomography and the QRI method are demonstrated.[A6, A7]

II. FORWARD AND BACKWARD PROCESSING OF THE ACOUSTICAL WAVE SCATTERING IN BIOLOGICAL SOFT TISSUES

1. Forward Processing of Acoustical Wave Scattering

Suppose the biological soft tissues can be modeled as static, isotropic and viscoelastic fluid medium, and the propagation of the acoustical wave in the medium is adiabatic, the rule which governs the propagation of the acoustical wave in the biological soft tissues can be described by the following system of nonlinear partial differential equations[10,11]:

(1) Equation of motion

$$\rho\left(\frac{\partial \underline{v}}{\partial t}\right)+\rho\underline{v}\cdot\nabla\underline{v} = \nabla\cdot\underline{\underline{\Im}}+\underline{E} \tag{2-1}$$

where $\rho = \rho(\underline{r},t)$ and $\underline{v} = \underline{v}(\underline{r},t)$ are the density of the medium and the vibrating velocity of the particles in the medium respectively; $\underline{E} = \underline{E}(\underline{r},t)$ is the net external force which acts on the medium; $\underline{\underline{\Im}}$ is a stress tensor, which is given by

$$\underline{\underline{\Im}} = -(u+\gamma\nabla\cdot\underline{v})\underline{\underline{\mathfrak{I}}}+\varepsilon(\nabla\underline{v}+\underline{v}\nabla) \tag{2-2}$$

where $u = u(\underline{r},t)$ is sound pressure; $\underline{\underline{\mathfrak{I}}}$ is a unit tensor; ε is viscous coefficient; $\gamma = (2/3)\varepsilon-\sigma$ is second friction coefficient, where σ is expansion friction coefficient; $\nabla\underline{v}$ is a tensor, and $\underline{v}\nabla$ represents the transposition of $\nabla\underline{v}$.

(2) Equation of continuity

$$\frac{\partial \rho}{\partial t} = -\nabla\cdot(\rho\underline{v}) \tag{2-3}$$

(3) Equation of state

$$\frac{\partial u}{\partial t} = \frac{\mathcal{K}}{\rho}\frac{d\rho}{dt} \tag{2-4}$$

where $\mathcal{K} = \mathcal{K}(\underline{r})$ is the adiabatic compression module.

Assume that the amplitude of incident acoustical wave is very small and there is no density fluctuation in the medium when the acoustical perturbation is absent. If the viscous coefficient ε and the friction coefficient σ are negligible, in the region beyond the sources of the sound the sound pressure u is satisfied by the following wave equation

$$\frac{\partial^2 u(\underline{r},t)}{\partial t^2} - C^2(\underline{r})\nabla^2 u(\underline{r},t) = 0 \tag{2-5}$$

where $C(\underline{r}) = \sqrt{\mathcal{K}(\underline{r})/\rho_0}$ represents the phase velocity of the acoustical wave

travelling in the medium, ρ_0 is the density of the medium with the absence of the acoustical perturbation.

For the sound pressure $u(\underline{r},t)$ can be expressed as a linear superposition of monochromatic wave with different frequency, the case that $u(\underline{r},t)$ is monochromatic will be considered first, i.e.

$$u(\underline{r},t) = U(\underline{r})\exp(-j\omega t) \tag{2-6}$$

where $U(\underline{r})$ is the amplitude of the monochromatic wave; ω represents the angular frequency.

Substituting Eq.(2-6) into Eq.(2-5), we have the following Helmholtz equation

$$\nabla^2 U(\underline{r})+K^2(\underline{r})U(\underline{r}) = 0 \tag{2-7}$$

where $K(\underline{r})$ is given by

$$K(\underline{r}) = \omega/C(\underline{r}) \tag{2-8}$$

The Helmholtz equation can be written in another form

$$\nabla^2 U(\underline{r})+k_0^2 U(\underline{r}) = -F(\underline{r})U(\underline{r}) \tag{2-9}$$

where $F(\underline{r})$ is the object function which represents the inhomogeneities of the distributions of the acoustical parameters of the object and is given by

$$F(\underline{r}) = \begin{cases} k_0^2[n^2(\underline{r})-1]; \text{ where } \underline{r} \text{ is a point in the object} \\ 0 \qquad\qquad ; \text{otherwise} \end{cases} \tag{2-10}$$

where $k_0 = \omega/C_0$ is the wavenumber of the medium surrounding the object; $n(\underline{r}) = C_0/C(\underline{r})$ represents the distribution of the refractive index of the object.

Suppose the volume which encircles the object is V_0 and the surface of the volume is S_0. Combining the partial differential equation shown in Eq.(2-9) with a boundary condition, the boundary-value problem which determines the distribution of the acoustical field $U(\underline{r})$ in the space will be formed. In practical medical imaging, the boundary conditions can be the combination of partly rigid and partly flexible boundary conditions[88]

$$\nabla_s U(\underline{r}_s)\cdot\underline{n}_s(\underline{r}_s)+e(\underline{r}_s)U(\underline{r}_s) = -h(\underline{r}_s) \tag{2-11}$$

where $e(\underline{r}_s)$ is the resistance reacting between the boundaries and their surrounding medium; $h(\underline{r}_s)$ is zero everywhere except on the source region; $\underline{n}_s(\underline{r}_s)$ represents the normal vector on the surface S_0 and is pointed to the inside of the volume V_0; ∇_s is the gradient in terms of $\underline{r}_s$, and $\underline{r}_s$ here is a position vector on the surface S_0.

In accordance with the boundary-value theory of the partial differential equation[101], the unique solution of the boundary-value problem which consists of Eq.(2-9) and Eq.(2-11) can be expressed as the summation of two parts: the solution of the inhomogeneous equation with the homogeneous boundary condition ($h(\underline{r}_s) = 0$) and the solution of the homogeneous equation ($F(\underline{r}) = 0$) with the inhomogeneous boundary condition. The solution of the inhomogeneous equation with the homogeneous boundary condition can be obtained by counting up every elementary contribution of the distribution sources in

the medium. If $G(\underline{r}|\underline{r}_0)$ is the field on the point $\underline{r}$ produced by a point source on $\underline{r}_0$, the field caused by the distribution source $F(\underline{r})U(\underline{r})$ will be the integration of the function $F(\underline{r}_0)U(\underline{r}_0)G(\underline{r}|\underline{r}_0)$ over the volume V_0. Here, $G(\underline{r}|\underline{r}_0)$ is the Green's function.

Similarly, the solution of the homogeneous equation with the inhomogeneous boundary condition can be obtained by counting up every elementary contribution of the boundary sources. To calculate the elementary contribution, $h(\underline{r}_s)$ will be set to zero everywhere except on the place where there is a source element. Therefore, each elementary contribution of the boundary sources will be the solution with the homogeneous boundary condition and with a point source on $\underline{r}_s$ on the boundaries. Such solution will be of the form of the above Green's function $G(\underline{r}|\underline{r}_0)$ where $\underline{r}_0 = \underline{r}_s$, and is notated as $G(\underline{r}|\underline{r}_s)$. Therefore, the field caused by the inhomogeneous boundary condition can be expressed as the integration of the function $G(\underline{r}|\underline{r}_0)h(\underline{r}_s)$ over the entire surface of the boundaries S_0.

In the following, the solution of the inhomogeneous equation (Eq.(2-9)) with the inhomogeneous boundary condition (Eq.(2-11)) will be given.

The Green's function $G(\underline{r}|\underline{r}_0)$ is satisfied by the following inhomogeneous Helmholtz equation and the homogeneous boundary condition

$$(\nabla^2+k^2_\delta)G(\underline{r}|\underline{r}_0) = -\delta(\underline{r}-\underline{r}_0) \tag{2-12a}$$

$$\nabla_s G(\underline{r}_s|\underline{r}_0)\cdot \underline{n}_s(\underline{r}_s)+e(\underline{r}_s)G(\underline{r}_s|\underline{r}_0) = 0 \tag{2-12b}$$

where $\delta(\underline{r}-\underline{r}_0)$ is the Dirac delta function which represents a point source on $\underline{r} = \underline{r}_0$. The Green's function $G(\underline{r}|\underline{r}_0)$ in Eq.(2-12) is continuous everywhere except on the singular point $\underline{r} = \underline{r}_0$, and when $|\underline{r}-\underline{r}_0| \to 0$,

$$G(\underline{r}|\underline{r}_0) \sim \frac{1}{|\underline{r}-\underline{r}_0|} \tag{2-13}$$

and it is proved that for the homogeneous boundary condition, $G(\underline{r}|\underline{r}_0)$ is symmetric

$$G(\underline{r}|\underline{r}_0) = G(\underline{r}_0|\underline{r}),\ \underline{r},\underline{r}_0 \in V_0 \tag{2-14}$$

Multiplying both side of Eq.(2-9) by $G(\underline{r}|\underline{r}_0)$ and both side of Eq.(2-12a) by $U(\underline{r})$ and then subtracting, we obtain

$$G(\underline{r}|\underline{r}_0)\nabla^2U(\underline{r})-U(\underline{r})\nabla^2G(\underline{r}|\underline{r}_0) = -F(\underline{r})U(\underline{r})G(\underline{r}|\underline{r}_0)+\delta(\underline{r}-\underline{r}_0)U(\underline{r}) \tag{2-15}$$

Exchanging the order of $\underline{r}$ and $\underline{r}_0$ in Eq.(2-15), and integrating the result in terms of $\underline{r}_0$ over the volume V_0, from the symmetry of $G(\underline{r}|\underline{r}_0)$ and $\delta(\underline{r}-\underline{r}_0)$, one obtains

$$\int_{V_0}[G(\underline{r}|\underline{r}_0)\nabla^2_\delta U(\underline{r}_0)-U(\underline{r}_0)\nabla^2_\delta G(\underline{r}|\underline{r}_0)]d\underline{r}_0 = -\int_{V_0}F(\underline{r}_0)U(\underline{r}_0)G(\underline{r}|\underline{r}_0)d\underline{r}_0 + \int_{V_0}U(\underline{r}_0)\delta(\underline{r}-\underline{r}_0)d\underline{r}_0 \tag{2-16}$$

where ∇^2_δ is the Laplacian operator with respect to $\underline{r}_0$. By the use of the Green's formula

$$\int_{V_0}[G(\underline{r}|\underline{r}_0)\nabla^2_\delta U(\underline{r}_0)-U(\underline{r}_0)\nabla^2_\delta G(\underline{r}|\underline{r}_0)]d\underline{r}_0 = \int_{S_0}[U(\underline{r}_s)\nabla_s G(\underline{r}|\underline{r}_s)-G(\underline{r}|\underline{r}_s)\nabla_s U(\underline{r}_s)]\cdot \underline{n}_s(\underline{r}_s)ds \tag{2-17}$$

the expression of the field on the point $\underline{r}$ in the volume V_0 can be obtained

$$U(\underline{r}) = \int_{V_0} F(\underline{r}_0)U(\underline{r}_0)G(\underline{r}|\underline{r}_0)d\underline{r}_0 + j_{S_0}[U(\underline{r}_s)v_s G(\underline{r}|\underline{r}_s) - G(\underline{r}|\underline{r}_s)v_s U(\underline{r}_s)]\cdot \underline{n}_s(\underline{r}_s)ds \quad (2\text{-}18)$$

where ds represents a differential area on S_0.

Substituting Eq.(2-12b) into Eq.(2-18), and using Eq.(2-11), one obtains

$$U(\underline{r}) = \int_{S_0} G(\underline{r}|\underline{r}_s)h(\underline{r}_s)ds + \int_{V_0} F(\underline{r}_0)U(\underline{r}_0)G(\underline{r}|\underline{r}_0)d\underline{r}_0 \quad (2\text{-}19)$$

Let

$$U_i(\underline{r}) = \int_{S_0} G(\underline{r}|\underline{r}_s)h(\underline{r}_s)ds \quad (2\text{-}20)$$

and

$$U_s(\underline{r}) = \int_{V_0} F(\underline{r}_0)U(\underline{r}_0)G(\underline{r}|\underline{r}_0)d\underline{r}_0 \quad (2\text{-}21)$$

one finds

$$U(\underline{r}) = U_i(\underline{r}) + U_s(\underline{r}) \quad (2\text{-}22)$$

where $U_i(\underline{r})$ is the field caused by the boundary sources when the object is homogeneous ($F(\underline{r}) = 0$), and therefore, it is called the incident field; $U_s(\underline{r})$ is the scattered field caused by the inhomogeneities ($F(\underline{r}) \neq 0$) of the object.

As the total field $U(\underline{r})$ is contained in Eq.(2-21), it is difficult in general to establish a simple relation between the object function and the scattered field. For in this paper, only the ultrasonic imaging of the biological soft tissues is concerned, the first-order approximation condition (weak scattering assumption) is satisfied. With the first-order approximation, a simple relationship between the object function and the measured scattered field can be established. So that, in the following, we will first find the integral solution of the scattered field under the condition of the first-order Born and the first-order Rytov approximation.

Substituting Eq.(2-22) into Eq.(2-21), one obtains

$$U_s(\underline{r}) = \int_{V_0} F(\underline{r}_0)U_i(\underline{r}_0)G(\underline{r}|\underline{r}_0)d\underline{r}_0 + \int_{V_0} F(\underline{r}_0)U_s(\underline{r}_0)G(\underline{r}|\underline{r}_0)d\underline{r}_0 \quad (2\text{-}23)$$

Let the first and the second term in Eq.(2-23) be $U_{s1}(\underline{r})$ and $\hat{U}_s(\underline{r})$ respectively. Then, substituting

$$U_s(\underline{r}) = U_{s1}(\underline{r}) + \hat{U}_s(\underline{r}) \quad (2\text{-}24)$$

into the expression of $\hat{U}_s(\underline{r})$, there will be

$$\hat{U}_s(\underline{r}) = \int_{V_0} F(\underline{r}_0)U_{s1}(\underline{r}_0)G(\underline{r}|\underline{r}_0)d\underline{r}_0 + \int_{V_0} F(\underline{r}_0)\hat{U}_s(\underline{r}_0)G(\underline{r}|\underline{r}_0)d\underline{r}_0 \quad (2\text{-}25)$$

Repeating the expansion procedure above and notating

$$U_{s(l+1)}(\underline{r}) = \int_{V_0} F(\underline{r}_0)U_{sl}(\underline{r}_0)G(\underline{r}|\underline{r}_0)d\underline{r}_0, \quad l \geq 1 \quad (2\text{-}26)$$

one obtains the Born solution

$$U(\underline{r}) = U_i(\underline{r}) + \sum_{l=1}^{\infty} U_{sl}(\underline{r}) \quad (2\text{-}27)$$

which is the series expansion solution of the wave equation Eq.(2-9). If the inhomogeneities of the object is very small, the series expansion solution will be convergent. The first N terms of the series is called Nth-order Born approximation solution of the wave equation Eq.(2-9) and, especially, when N = 1, is called the first-order Born approximation solution

$$U(\underline{r}) = U_i(\underline{r}) + U_{s1}(\underline{r}) \tag{2-28}$$

or

$$U_s(\underline{r}) = U_{s1}(\underline{r}) = \int_{V_0} F(\underline{r}_0) U_i(\underline{r}_0) G(\underline{r}|\underline{r}_0) d\underline{r}_0 \tag{2-29}$$

The equation above can be obtained from Eq.(2-21) directly, provided that $U(\underline{r})$ is replaced by $U_i(\underline{r})$. Therefore, the first-order Born approximation requires that $|U_s(\underline{r})| << |U_i(\underline{r})|$, i.e., the scattered field should be much smaller than the incident field.

If

$$U(\underline{r}) = \exp[\psi(\underline{r})] \tag{2-30}$$

from Eq.(2-9), we obtain the Riccati equation

$$\nabla^2\psi(\underline{r}) + \nabla\psi(\underline{r}) \cdot \nabla\psi(\underline{r}) + k^2 = -F(\underline{r}) \tag{2-31}$$

The solution of this equation can be expressed as the sum of two terms[27]

$$\psi(\underline{r}) = \psi_i(\underline{r}) + \psi_s(\underline{r}) \tag{2-32}$$

where $\psi_i(\underline{r})$ is the solution of Eq.(2-31) when $F(\underline{r}) = 0$, and is given by

$$U_i(\underline{r}) = \exp[\psi_i(\underline{r})] \tag{2-33}$$

Substituting Eq.(2-32) into Eq.(2-31) and considering the equation

$$\nabla^2\psi_i(\underline{r}) + \nabla\psi_i(\underline{r}) \cdot \nabla\psi_i(\underline{r}) + k^2 = 0 \tag{2-34}$$

we obtain

$$\nabla^2\psi_s(\underline{r}) + 2\nabla\psi_i(\underline{r}) \cdot \nabla\psi_s(\underline{r}) = -\nabla\psi_s(\underline{r}) \cdot \nabla\psi_s(\underline{r}) - F(\underline{r}) \tag{2-35}$$

Multiplying both sides of Eq.(2-35) with $U_i(\underline{r})$ and noticing that

$$\nabla^2 U_i(\underline{r}) = -k^2 U_i(\underline{r}) \tag{2-36}$$

we obtain the following equation

$$(\nabla^2 + k^2)(U_i(\underline{r})\psi_s(\underline{r})) = -[F(\underline{r}) + \nabla\psi_s(\underline{r}) \cdot \nabla\psi_s(\underline{r})] U_i(\underline{r}) \tag{2-37}$$

Eq.(2-37) is the inhomogeneous Helmholtz equation. Likewise, with the replace of $F(\underline{r})U(\underline{r})$ in Eq.(2-21) by $[F(\underline{r}) + \nabla\psi_s(\underline{r}) \cdot \nabla\psi_s(\underline{r})]U_i(\underline{r})$, the solution of Eq.(2-37) will be obtained

$$\psi_s(\underline{r}) = \psi_{s1}(\underline{r}) + \hat{\psi}_{s2}(\underline{r}) \tag{2-38}$$

where

$$\psi_{s1}(\underline{r}) = \frac{1}{U_i(\underline{r})}\int_{V_0} F(\underline{r}_0)U_i(\underline{r}_0)G(\underline{r}|\underline{r}_0)d\underline{r}_0 \tag{2-39}$$

and

$$\psi_{s2}(\underline{r}) = \frac{1}{U_i(\underline{r})}\int_{V_0} \nabla\psi_s(\underline{r}_0)\cdot\nabla\psi_s(\underline{r}_0)U_i(\underline{r}_0)G(\underline{r}|\underline{r}_0)d\underline{r}_0 \tag{2-40}$$

Expanding repeatedly the right hand side of Eq.(2-40), the series expansion solution of the Riccati equation will be found. Similarly, such solution is called Rytov solution. Again, if the inhomogeneities of the object are small, the Rytov solution will be convergent. The first-order Rytov approximation is given by

$$\psi(\underline{r}) = \psi_i(\underline{r})+\psi_{s1}(\underline{r}) \tag{2-41}$$

i.e.

$$\psi_s(\underline{r}) = \psi_{s1}(\underline{r}) = \frac{1}{U_i(\underline{r})}\int_{V_0} F(\underline{r}_0)U_i(\underline{r}_0)G(\underline{r}|\underline{r}_0)d\underline{r}_0 \tag{2-42}$$

From Eq.(2-42), it is seen that the first-order Rytov approximation requires that $|\nabla\psi_s(\underline{r})\cdot\nabla\psi_s(\underline{r})| << |F(\underline{r})|$, that is, the rate of the spatial variation of the phase of the scattered field must be very small. If $\psi_s(\underline{r})U_i(\underline{r})$ is treated as a new field variable, Eq.(2-42) has the same form as Eq.(2-29), i.e., the integral expressions of the Born and Rytov solution has the same form provided that the first-order approximation condition is satisfied. Therefore, it is enough to study the inverse scattering problem of Eq.(2-29) which is obtained from the first-order Born approximation.

Suppose $G(\underline{r}|\underline{r}_0)$ in Eq.(2-29) is a free-space Green's function, then it is given by[101]

$$G(\underline{r}|\underline{r}_0) = \frac{\exp(jk_0|\underline{r}-\underline{r}_0|)}{|\underline{r}-\underline{r}_0|} \tag{2-43}$$

where $|\underline{r}-\underline{r}_0|$ is the Euclidean distance between the field point $\underline{r} = (x,y,z)$ and the source point $\underline{r}_0 = (x_0,y_0,z_0)$.

In what follows, only the two-dimensional case (i.e., the variation of the object function along the z axis is assumed to be very small, and the both the incident and the scattered fields are independent of the z axis) is studied. Then, the Green's function can be written[102]

$$g(\underline{r}|\underline{r}_0) = \frac{j}{4}H_0(k_0|\underline{r}-\underline{r}_0|) \tag{2-44}$$

where H_0 is zeroth-order Hankel function with the first kind. By angular expansion of the Hankel function, we can obtained

$$H_0(k_0|\underline{r}-\underline{r}_0|) = \frac{1}{\pi}\int_{-\infty}^{+\infty}\frac{\exp(j\underline{K}\cdot(\underline{r}-\underline{r}_0))}{K_y}dK_x \tag{2-45}$$

where $\underline{K} = (K_x, K_y)$, and

$$K_y = \sqrt{k_0^2 - K_x^2} \tag{2-46}$$

Then, Eq.(2-29) can be written in an alternate form

$$U_s(\underline{r}) = \int_s F(\underline{r}_0) U_i(\underline{r}_0) g(\underline{r}|\underline{r}_0) d\underline{r}_0 \tag{2-47}$$

where the integral area s contains the cross-section of the object; and $\underline{r} = (x,y)$, $\underline{r}_0 = (x_0, y_0)$. Eq.(2-47) is taken as the basic equation for the study in this paper.

2. Backward Processing of the Acoustical Wave Scattering

Let us consider the datum acquisition geometry of the diffraction tomography (see Fig.(2-1)). Where $F(\underline{r})$ represents the two-dimensional object function; $\underline{r} = (x,y)$ is a position vector in the space; $y_1 = l_0$ is the moving line of the receiver. Together with the transmitter, this line is fixed on the x_1-y_1 coordinates and can be rotated around the object from 0° to 360°; Θ and Θ_1 represent the angles between the y_1 axis and the x_1 axis and between the y_1 axis and the x axis respectively, besides, $\Theta = \Theta_1 + \pi/2$. Assume that the incident wave is a plane wave travelling along the positive direction of the y_1 axis, and is given by

$$U_i(\underline{r}) = U_0 \exp(jk_0 \underline{s}_0 \cdot \underline{r}) \tag{2-48}$$

where $\underline{s}_0$ is the unit vector on the direction of the plane wave insonification; U_0 is the complex amplitude of the plane wave (without losing generality, we assume that $U_0 = 1$).

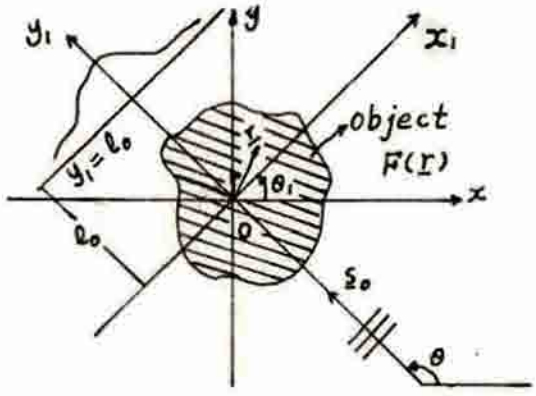

Fig.(2-1) Datum acquisition geometry of the diffraction tomography

Substituting Eq.(2-44) and Eq.(2-48) into Eq.(2-47) and using Eq.(2-45), it is easy to show

$$U_s(\underline{r}) = \frac{j}{4\pi} \int_{-\infty}^{+\infty} \frac{\exp(j\underline{K}\cdot\underline{r})}{K_y} \tilde{F}(\underline{K} - k_0 \underline{s}_0) dK_x \tag{4-49}$$

where

$$\tilde{F}(\underline{K} - k_0 \underline{s}_0) = \int_s F(\underline{r}_0) \exp[-j(\underline{K} - k_0 \underline{s}_0)\cdot \underline{r}_0] d\underline{r}_0 \tag{2-50}$$

Let us define

$$Q = \begin{bmatrix} \cos\theta_1 & -\sin\theta_1 \\ \sin\theta_1 & \cos\theta_1 \end{bmatrix} \tag{2-51}$$

and make the following variable transformations

$$\underline{r} = Q\underline{r}_1 \tag{2-52}$$

$$\underline{K} = \underline{T}Q^{-1} \tag{2-53}$$

where $\underline{r}_0$ and $\underline{r}_1$ are column vectors; $\underline{K}$ and $\underline{T}$ are row vectors; Q^{-1} is the inversion of Q; $\underline{r}_1 = (x_1, y_1) = [x_1, y_1]^t$, where the superscript t represents the transposition of the vector; and $\underline{T} = (t_x, t_y)$. From Eq.(2-53), it is easy shown that

$$\begin{cases} K_x = t_x\cos\theta_1 - t_y\sin\theta_1 \\ K_y = t_x\sin\theta_1 + t_y\cos\theta_1 \end{cases} \tag{2-54}$$

Using Eq.(2-46) and summing the square of K_x and the square of K_y in Eq.(2-54), one obtains

$$t_y = \sqrt{k_0^2 - t_x^2} \tag{2-55}$$

Differentiating K_x in Eq.(2-54) in terms of t_x results in

$$dK_x = [\cos\theta_1 + \frac{t_x}{t_y}\sin\theta_1]dt_x \tag{2-56}$$

From the expression of K_y in Eq.(2-54), we can see that

$$t_x\sin\theta_1 = K_y - t_y\cos\theta_1 \tag{2-57}$$

By substituting Eq.(2-57) into Eq.(2-56), the differential of K_x is obtained

$$dK_x = \frac{K_y}{t_y}dt_x \tag{2-58}$$

Decomposing the vector $\underline{s}_0$ in Fig.(2-1) along the x and the y axis, one finds

$$\begin{aligned} \underline{s}_0 &= \cos(\theta_1 + \pi/2)\underline{i} + \sin(\theta_1 + \pi/2)\underline{j} \\ &= -\sin\theta_1\underline{i} + \cos\theta_1\underline{j} \end{aligned} \tag{2-59}$$

where $\underline{i}$ and $\underline{j}$ are the unit vectors on the x and the y axis respectively.

Decomposing the vector $\underline{K} - k_0\underline{s}_0$ in Eq.(2-49) along the x and the y axis and using Eq.(2-54), we have

$$\underline{K} - k_0\underline{s}_0 = u\underline{i} + v\underline{j} \tag{2-60}$$

where

$$\begin{cases} u = t_x\cos\theta_1 - (t_y - k_0)\sin\theta_1 \\ v = t_x\sin\theta_1 + (t_y - k_0)\cos\theta_1 \end{cases} \tag{2-61}$$

With Eq.(2-51), Eq.(2-60) can be rewritten in a vector form

$$\underline{K}-k_0\underline{s}_0 = (\underline{T}-k_0\underline{s}_0)Q^{-1} \tag{2-62}$$

From Eq.(2-52) and Eq.(2-53), one shows that

$$j\underline{K}\cdot\underline{r} = j\underline{T}Q^{-1}\cdot Q\underline{r}_1 = j\underline{T}\cdot\underline{r}_1 \tag{2-63}$$

Substituting Eq.(2-58), Eq.(2-62) and Eq.(2-63) into Eq.(2-49), we obtain in x_1-y_1 coordinates the expression of the scattered field

$$U_s(\underline{r}_1) = \frac{j}{4\pi}\int_{-\infty}^{+\infty}\frac{\exp(j\underline{T}\cdot\underline{r}_1)}{t_y}\tilde{F}[(\underline{T}-k_0\underline{s}_0)Q^{-1}]dt_x \tag{2-64}$$

Setting $y_1 = l_0$ and taking the Fourier transform of $U_s(\underline{r}_1)$ with respect to the variable x_1, from Eq.(2-64) we find the relationship between the Fourier transform of the measured scattered field and the Fourier transform of the object function, i.e., the so-called diffraction-projection theorem

$$\tilde{U}_s(t_x,\theta) = \frac{j\exp(jt_y l_0)}{2t_y}\tilde{F}[(\underline{T}-k_0\underline{s}_0)Q^{-1}] \tag{2-65}$$

From Eq.(2-65), it is easy to recover the object function $F(\underline{r})$, that is, to find the solution of the inverse scattering problem. The filtered-backpropagation algorithm for solving $F(\underline{r})$ was put forward by A.J. Devaney in 1982

$$F(\underline{r}) = \frac{1}{2\pi}\int_0^{2\pi}\prod_\theta(x\sin\theta-y\cos\theta, x\cos\theta+y\sin\theta)d\theta \tag{2-66}$$

where

$$\prod_\theta(x_1,y_1) = -\frac{k\delta}{2\pi}\int_{-k_0}^{+k_0}\Gamma(t_x,\theta)H(t_x)G(t_x,y_1)\exp(jt_x x_1)dt_x \tag{2-67}$$

and where

$$\Gamma(t_x,\theta) = j\exp(-jk_0 l_0)\tilde{U}_s(t_x,\theta)/k_0 \tag{2-68}$$

$$H(t_x) = \begin{cases} |t_x|; & |t_x| \leqslant k_0 \\ 0 \quad ; & \text{otherwise} \end{cases} \tag{2-69}$$

$$G(t_x,y_1) = \begin{cases} \exp[j(t_y-k_0)(y_1-l_0)]; & |t_x| \leqslant k_0 \\ 0 \qquad\qquad\qquad\quad ; & \text{otherwise} \end{cases} \tag{2-70}$$

As there is a space-variant filter function in $G(t_x,y_1)$, the Devaney's algorithm above requires vast amount of computation. In what follows, we will first speed up the Pan's algorithm which has reduced the computation of the Devaney's algorithm obviously. Then, some reconstruction algorithms of the diffraction tomography with different datum acquisition geometries will be studied further for the improvement of their speed and the quality.

III. A STUDY OF RECONSTRUCTION ALGORITHMS OF DIFFRACTION TOMOGRAPHY

1. Application of Cubic Spline Interpolation to Densifying of Diffracted Data of Diffraction Tomography

(1) Zero-padding technique and spline algorithm

Zero-padding technique

In practical datum acquisition, the scattered field $U_s(t_x,\theta)$ is known only on some discrete values of its variables t_x and θ. The stepping lengths of t_x and θ are usually large because of the restriction of the physical system. Therefore, the resolution of the interpolation in the image reconstruction using Fourier-domain interpolation algorithm will be poor if the known points of the scattered field are not increased. Hence, to reconstruct high quality images, it is necessary to densifying the diffracted data using some interpolation schemes, i.e., to increase the known points of the Fourier transform of the object function on the curvilinear coordinates $\{(\underline{T}-k_0\underline{s}_0)Q^{-1};\ \underline{T}=(t_x,t_y),\ t_y=\sqrt{k_0^2-t_x^2},\ |t_x|\leq k_0\}$. If $U_s(t_x,\theta)$ is discretized with fixed stepping lengths for both t_x and θ, the zero-padding technique[91] can be used for the densifying of the diffracted data. The densifying procedure is as follows: Suppose there is a one-dimensional N-point sequence with a fixed stepping length of h, $y(n)$, $n=0,1,2,\cdots,N-1$. Taking the N-point FFT of this sequence, one will obtain the N-point spectrum, $Y(k)$, $K=0,1,2,\cdots,N-1$. To densifying the sequence $y(n)$ to L times (L is an integer), it is necessary to insert (L-1)N zeros into the high-frequency portion of the spectrum. Notating the zero-extended spectrum as $X(k')$, $k'=0,1,2,\cdots,LN-1$, it is easy to show that

$$X(k')=\begin{cases} Y(k') & ;\ 0\leq k'\leq N/2-1 \\ 0 & ;\ N/2\leq k'\leq LN-N/2-1 \\ Y(k'-LN+N) & ;\ LN-N/2\leq k'\leq LN-1 \end{cases} \tag{3-1}$$

Taking the LN-point IFFT of the spectrum, one can obtain the densified sequence $x(n')$ which is L times lengthened when compared with the original sequence $y(n)$

$$x(n')=\frac{1}{LN}\sum_{k'=0}^{LN-1}X(k')\exp[j(2\pi/LN)n'k']$$

$$=\frac{1}{LN}\Big\{\sum_{k=0}^{N/2-1}Y(k)\exp[j(2\pi/LN)n'k]+\sum_{k=N/2}^{N-1}Y(k)\exp[j(2\pi/LN)n'k]$$

$$\cdot\exp[j(2\pi/LN)(L-1)Nn']\},\ (n'=0,1,2,\cdots,LN-1) \tag{3-2}$$

Let $n'=Ln$, the equation above becomes

$$x(Ln)=\frac{1}{LN}\Big\{\sum_{k=0}^{N/2-1}Y(k)\exp[j(2\pi/LN)Lnk]+\sum_{k=N/2}^{N-1}Y(k)\exp[j(2\pi/LN)Lnk]\Big\}$$

$$= \frac{1}{L}\left\{\frac{1}{N}\sum_{k=0}^{N-1} Y(k)\exp[j(2\pi/N)nk]\right\} = \frac{1}{L}y(n) \qquad (3\text{-}3)$$

i.e.

$$x(Ln) = \frac{1}{L}y(n) \qquad (3\text{-}4)$$

It is seen from Eq.(3-4) that the densified sequence keeps linearly unchanged on the points of the original sequence, and between each successive two points of the densified sequence, L-1 points are inserted. The basic idea of the zero-padding technique for densifying a sequence is that the shapes of the spectra of the sequence before and after the densification are kept the same. The densifying procedure above for the one-dimensional sequence can be easily extended to the two-dimensional case.

Spline algorithm

It can be seen that the zero-padding technique above requires still a lot of computation, for in this technique LN-point IFFT of the LN-point zero-extended spectrum must be taken. For instance, for a 128x128 pixel image reconstructed from the densified 64x128 diffracted data, the time for the densifying of the diffracted data is about 63% of the total time of the image reconstruction. In order to reduce the time for the densifying of the diffracted data, cubic spline interpolation is used.

The cubic spline interpolation is a high precision interpolation method, but it is usually complex and time-consumed[104]. However, when applied in the mid-point interpolation of a sequence with a fixed stepping length, which is the case for the densifying of the diffracted data, it is less complicated and requires less amount of computation. In the following, the procedure for the densifying of a one-dimension sequence using cubic spline interpolation will be given in detail. As before, the densifying procedure for one-dimensional sequence can be extended to the two-dimensional case directly.

If $S(x)\ C^2[a,b]$ (i.e., the second-order differential of S(x) is continuous in internal [a,b] and S(x) is the polynomial of degree three in each subinterval $[x_n, x_{n+1}]$ (where $a = x_1 < x_2 < \cdots < x_N = b$ is the given nodes of S(x), S(x) is called the cubic spline function on nodes $x_1, x_2, \cdots, x_N$. If the value y(n) is given to S(x) on the node x_n, $n = 1,2,\cdots,N$, so that

$$S(x_n) = y_n, \quad (n = 1,2,\cdots,N) \qquad (3\text{-}5)$$

S(x) is called cubic spline interpolation function.

From the cubic Hermite interpolation function, the expression of S(x) in the subinterval $[x_n, x_{n+1}]$ can be derived[105].

$$S(x) = \frac{(x-x_{n+1})^2[h_n+2(x-x_n)]}{h_n^3}y(n) + \frac{(x-x_n)^2[h_n+2(x_{n+1}-x)]}{h_n^3}y(n+1)$$

$$+\frac{(x-x_{n+1})^2(x-x_n)}{h_n^2}m_n + \frac{(x-x_n)^2(x-x_{n+1})}{h_n^2}m_{n+1} \qquad (3\text{-}6)$$

where $h_n = x_{n+1}-x_n$; and m_n represents the first-order derivative of S(x) on

the node x_n. With the condition that the second-order differential of S(x) on the node x_n are continuous, $n = 2,3,\cdots,N-1$, one will see that m_n satisfies the following system of linear algebraic equations

$$\lambda_n m_{n-1} + 2m_n + \mu_n m_{n+1} = g_n, \quad (n = 2,3,\cdots,N-1) \tag{3-7}$$

where

$$\lambda_n = \frac{h_n}{h_{n-1}+h_n} \tag{3-8}$$

$$\mu_n = \frac{h_{n-1}}{h_{n-1}+h_n} \tag{3-9}$$

$$g_n = 3\left[\lambda_n \frac{y(n)-y(n-1)}{h_{n-1}} + \mu_n \frac{y(n+1)-y(n)}{h_n}\right] \tag{3-10}$$

Considering the nature end-point condition

$$S''(x_1) = S''(x_N) = 0 \tag{3-11}$$

we obtain the end-point equations for m_1 and m_N

$$\begin{cases} 2m_1 + m_2 = g_1 \\ m_{N-1} + 2m_N = g_N \end{cases} \tag{3-12}$$

where

$$g_1 = 3\frac{y(2)-y(1)}{h_1} \tag{3-13}$$

$$g_N = 3\frac{y(N)-y(N-1)}{h_{N-1}} \tag{3-14}$$

Suppose y(n) is a N-point sequence with fixed stepping length of h. If the cubic spline function is used for the mid-point interpolation of y(n) in the subinterval $[x_n, x_{n+1}]$, the cubic spline function will be of a simple form

$$S(x_n + \frac{h}{2}) = \frac{1}{2}[y(n)+y(n+1)] + \frac{h}{8}(m_n - m_{n+1}) \quad (n = 1,2,\cdots,N-1) \tag{3-15}$$

where m_n satisfies the following systems of linear algebraic equations

$$\begin{cases} \frac{1}{2}m_{n-1} + 2m_n + \frac{1}{2}m_{n+1} = g_n \quad (n = 2,3,\cdots,N-1) \\ 2m_1 + m_2 = g_1 \\ m_{N-1} + 2m_N = g_N \end{cases} \tag{3-16}$$

which is simplified from Eq.(3-7) and Eq.(3-12), where

$$\begin{cases} g_n = \dfrac{3}{2h}[y(n+1)-y(n-1)], \ (n = 2,3,\cdots,N-1) \\ g_1 = \dfrac{3}{h}[y(2)-y(1)] \\ g_N = \dfrac{3}{h}[y(N)-y(N-1)] \end{cases} \tag{3-17}$$

Eq.(3-16) can be rewritten in a matrix form

$$\mathbf{A}\,\mathbf{M} = \mathbf{g} \tag{3-18}$$

where

$$\mathbf{A} = \begin{bmatrix} 2 & 1 & 0 & \cdots & 0 & 0 & 0 \\ 1/2 & 2 & 1/2 & \cdots & 0 & 0 & 0 \\ 0 & 1/2 & 2 & \cdots & 0 & 0 & 0 \\ \cdots & \cdots & \cdots & \cdots & \cdots & \cdots & \cdots \\ 0 & 0 & 0 & \cdots & 1/2 & 2 & 1/2 \\ 0 & 0 & 0 & \cdots & 0 & 1 & 2 \end{bmatrix} \tag{3-19}$$

$\mathbf{M} = (m_1, m_2, \cdots, m_N)^t$ and $\mathbf{g} = (g_1, g_2, \cdots, g_N)^t$, where the superscript t represents the transposition of the vectors.

From the coefficient matrix Eq.(3-19), it can be seen that Eq.(3-18) is a diagonal dominant tridiagonal system. Therefore, Eq.(3-18) has a unique solution and can be solved by the following method[105]

(1) Find auxiliary parameter b_n

$$\begin{cases} b_1 = 1/2 \\ b_n = 1/(4-b_{n-1}), \ (n = 2,3,\cdots,N-1) \end{cases} \tag{3-20}$$

(2) Calculate another auxiliary parameter a_n

$$\begin{cases} a_1 = (1/2)g_1 \\ a_n = (2g_n - a_{n-1})b_n \\ a_N = (g_N - a_{N-1})/(2-b_{N-1}), \ (n = 2,3,\cdots,N-1) \end{cases} \tag{3-21}$$

(3) Determine m_n from a_n and b_n

$$\begin{cases} m_N = a_N \\ m_n = a_n - b_n m_{n+1}, \ (n = N-1,\cdots,2,1) \end{cases} \tag{3-22}$$

Substituting m_n obtained above into Eq.(3-15), one finds the sequence which is two-times longer than the original one. If $n = N$, we set $S(x_N+h/2) = S(x_N-h/2)$. The lengthened sequence can be further densified provided that the lengthened sequence is taken as the original sequence and the densifying procedure above is repeated. As a contrast, for a 128x128 pixel image reconstructed from the 8-fold densified 64x128 diffracted data, the time used now is only about 29% of that used by the complete image reconstruction.

(2) Computer simulations

(b) Gray level assignments

Fig.(3-1) is the head phantom used in our computer simulations. Fig.(3-1)(a) is the 128x128 pixel photograph of the phantom taken from the screen of monitor, and Fig.(3-1)(b) is the gray level assignments of Fig.(3-1)(a). The line $y = -0.605$ in Fig.(3-1)(b) passes through three smallest ellipses in the phantom and hence, the reconstructed values on this line can be used for the evaluation of the resolution and then the quality of the reconstructed images. Therefore, in our computer simulations hereafter, the comparisons between the reconstructed values and the gray level of the phantom on this line for all reconstructed images will be given.

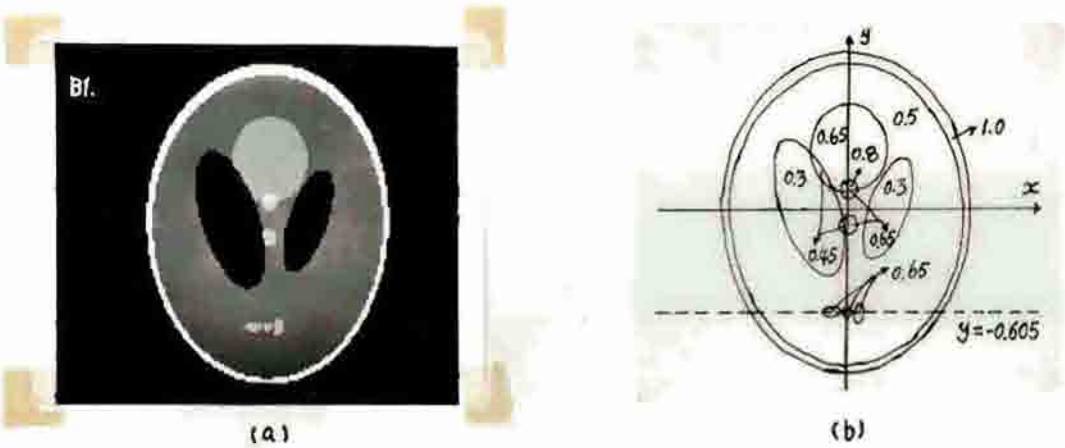

Fig.(3-1) (a) The head phantom used in our computer simulations (a) Photograph (b) Gray level assignments

In order to evaluate the quality of the reconstructed images quantitatively, it is necessary to find an objective evaluation standard. Unfortunately, there is no a generally accepted standard at present. In this paper, three picture distance measures which are in common use are adopted: normalized root mean squared picture distance measures d_1, normalized mean absolute picture distance measures r_1 and worst case picture distance measures e_1[37]. The definition of these picture distance measures for a NxN pixel image is as follows

$$d_1 = \frac{\sum_{i=1}^{N}\sum_{j=1}^{N}(r_{ij}-p_{ij})^2}{\sum_{i=1}^{N}\sum_{j=1}^{N}(p_{ij}-\bar{p})^2} \tag{3-23}$$

$$r_1 = \frac{\sum_{i=1}^{N}\sum_{j=1}^{N}|r_{ij}-p_{ij}|}{\sum_{i=1}^{N}\sum_{j=1}^{N}|p_{ij}|} \tag{3-24}$$

$$e_1 = \max_{\substack{1\leq I\leq N/2\\ 1\leq J\leq N/2}} |R_{IJ}-P_{IJ}| \tag{3-25}$$

where

$$R_{I,J} = \frac{1}{4}(r_{2I,2J}+r_{2I+1,2J}+r_{2I,2J+1}+r_{2I+1,2J+1}) \tag{3-26a}$$

$$P_{I,J} = \frac{1}{4}(p_{2I,2J}+p_{2I+1,2J}+p_{2I,2J+1}+p_{2I+1,2J+1}) \tag{3-26b}$$

$$(I,J = 1,2,3,\cdots,N/2)$$

$r_{i,j}$ and $p_{i,j}$ in above equations represent the gray level of the pixel on the ith row and the jth column of the reconstructed images and the phantom respectively; $\bar{r}$ and $\bar{p}$ are the averages of the gray level of the reconstructed images and the phantom respectively, and they are defined by

$$\bar{r} = \frac{1}{N^2}\sum_{i=1}^{N}\sum_{j=1}^{N} r_{i,j} \tag{3-27}$$

$$\bar{p} = \frac{1}{N^2}\sum_{i=1}^{N}\sum_{j=1}^{N} p_{i,j} \tag{3-28}$$

The above three picture distance measures reflect the different aspects of the errors of the reconstructed images: d_1 is sensitive to the big errors on individual points, r_1 relates the accumulation of small errors, and e_1 indicates the maximum error of the elements ($R_{I,J}$) of the reconstructed images.

If the averages of the reconstructed images are different from that of the phantom, average adjusted picture distance measures can be used for the quantitative evaluation of the quality of the reconstructed images[A3], The average adjusted picture distance measures are calculated in the following way: First, the averages of the reconstructed images and the phantom must be found from Eq.(3-27) and Eq.(3-28) respectively, then, the difference between r and p is added to every pixel of the reconstructed images. Finally, the picture distance measures d_1, r_1 and e_1 of the average adjusted images are calculated using Eq.(3-23) to Eq.(3-25) and are notated as d_2, r_2 and e_2 respectively. From the definitions of the average adjusted picture distance measures, it is seen that for these picture distance measures get rid of the factor that the averages of the reconstructed images are different from that of the phantom, they will reflect better the quality of the reconstructed images shown on the monitor screen (the brightness of the monitor, i.e., the averages of the reconstructed images shown on the monitor screen, can be adjusted arbitrarily). If the reconstructed images are the phantom itself, it is easy to show that all the picture distance measures will be zeros. Therefore, the higher the quality of the reconstructed images is, the smaller the picture distance measures of these images will be. Moreover, for the comparisons of the maximum and the minimum gray level of the reconstructed images with those of the phantom respectively, the maximum and minimum reconstructed values of the reconstructed images, max and min, are given (the maximum and the minimum gray level of the phantom are 1.0 and 0.0 respectively).

Fig.(3-2)(a) is a 128x128 pixel image reconstructed directly from the 64x128 diffracted data. Fig.(3-3)(a) and Fig.(3-4)(a) are the 128x128 pixel images reconstructed with the diffracted data densified from 64x128 to 128x512 using the zero-padding technique and the cubic spline interpolation respectively. Fig.(3-2)(b) to Fig.(3-4)(b) are the figures of the comparisons of the reconstructed values (real line) and the real values (dashed line) on the line $y = -0.605$ (see Fig.(3-1)(b)) corresponding to Fig.(3-2)(a) to

Fig.(3-4)(a), respectively. Table (3-1) shows the comparisons of the "distances" of the reconstructed images and gives the CPU processing time t and t' of the VAX-11/730 computer for the image reconstruction and for the densifying of the diffracted data respectively.

The computer simulations above show that: 1) the quality of the images reconstructed by the densifying of the diffracted data (see Fig.(3-3)(a) and Fig.(3-4)(a)) is much higher than that of the image reconstructed directly from the diffracted data without densifying (see Fig.(3-2)(a)). 2) The quality of the image reconstructed by the spline algorithm is comparable to that of the image reconstructed by the Pan's algorithm (the densifying of the diffracted data using the zero-padding technique). 3) The computer CPU processing time taken by the image reconstruction using spline algorithm is about 1/2 of that taken by the image reconstruction using the Pan's algorithm, and the time for the densifying of the diffracted data using the spline algorithm is only about 1/4 of that when using the Pan's algorithm (it is worth noticing that the longer the densified diffracted data is, the smaller the ratio of the CPU processing time for the densifying of the diffracted data between the spline and Pan's algorithm will be). Therefore, the spline algorithm is a more effective method for the image reconstruction of the diffraction tomography.

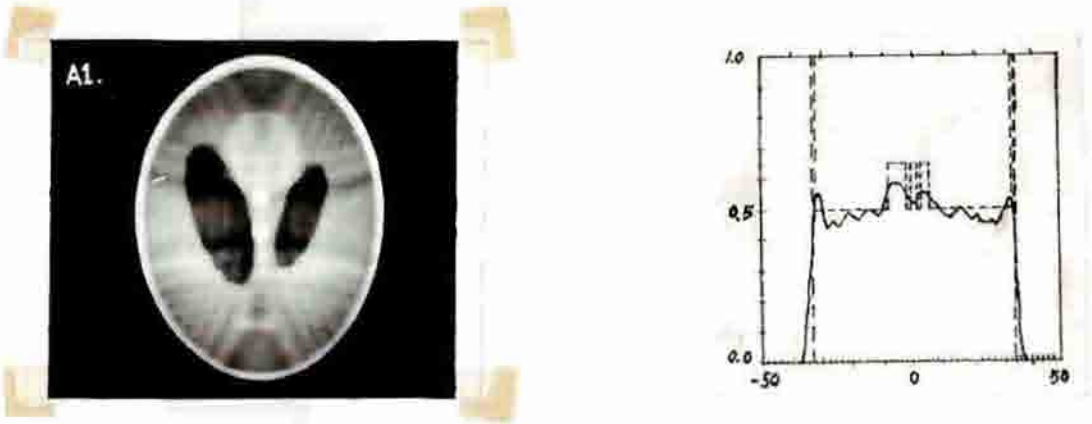

(a) (b)

Fig.(3-2) (a) 128x128 pixel image reconstructed from 64x128 diffracted data directly (without the densifying of the diffracted data) (b) The comparison of the reconstructed values (real line) and the real values (dashed line) on the line y = -0.605 (see Fig.(3-1)(b))

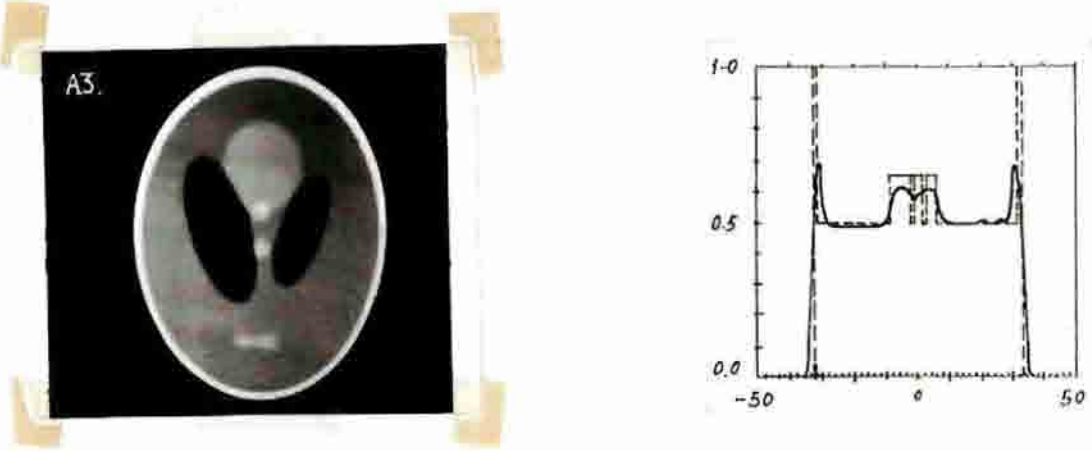

(a) (b)

Fig.(3-3) (a) 128x128 pixel image reconstructed with the diffracted data densified from 64x128 to 128x512 using the zero-padding technique (b) The comparison of the reconstructed values (real line) and the real values (dashed line) on the line y = -0.605 (see Fig.(3-1)(b))

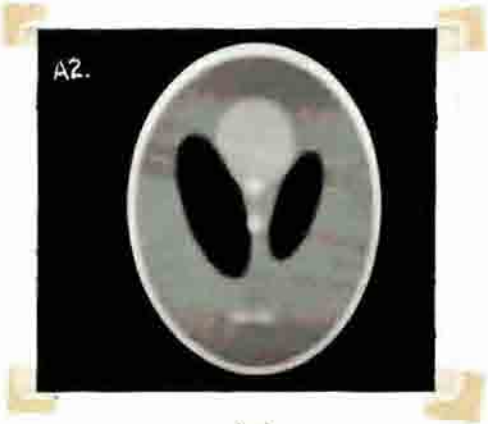

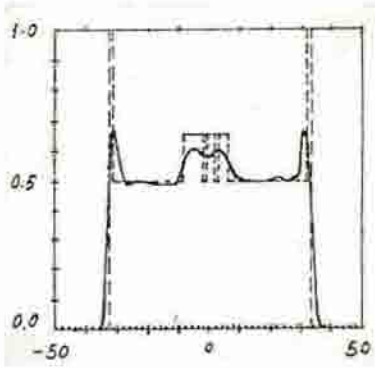

(a) (b)

Fig.(3-4) (a) 128x128 pixel image reconstructed with the diffracted data densified from 64x128 to 128x512 using the spline algorithm (b) The comparison of the reconstructed values (real line) and the real values (dashed line) on the line $y = -0.605$ (see Fig.(3-1(b))

Table (3-1) Distance measures of the reconstructed images and the computer CPU processing times for the reconstructions and for the densifying of the diffracted data

Figure	Specifications	d_1	r_1	e_1	d_2	r_2	e_2	max	min	t	t'
(3-2)	No densifying	.36	.20	.53	.36	.20	.53	.80	$-.85\times10^{-1}$	1.5	0.0
(3-3)	Zero-padding	.28	.11	.39	.28	.11	.39	.97	$-.22\times10^{-1}$	4.1	2.6
(3-4)	Cubic spline	.29	.12	.41	.29	.12	.41	.94	$-.31\times10^{-1}$	2.1	0.6

2. Transmission-Reflection Diffraction Tomography

(1) Diffraction-projection formulas and relationships between rectangular and curvilinear coordinates

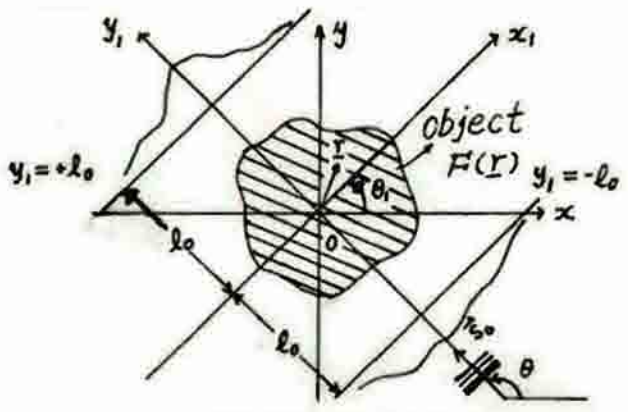

Fig.(3-5) Datum acquisition system of the TRDCT

Fig.(3-5) is the datum acquisition system of the TRDCT, it is the same as Fig.(2-1) except that the transmitter is also taken as the receiver and is located at the line $y_1 = -l_0$. In order to receive the transmission and the reflection waves simultaneously, a pseudo-continuous wave must be generated,

i.e., a sinusoidal wave chain generated must be so long that it may be looked as a continuous wave, but will be not too long that the measurement of the reflection wave is affected. This condition can be satisfied by properly adjusting the length of the sinusoidal wave chain and the distance l_0. In the datum acquisition, for each given Θ, 2N samples can be obtained by two transducers on the lines $y_1 = +l_0$ and $y_1 = -l_0$ respectively. If Θ changes from 0^0 to 360^0 by N angles, 2(NxN) diffracted data can be acquired. From the 2(NxN) diffracted data, object function can be reconstructed by the TRDCT.

The diffraction-projection formula for the transmission signal is the same as Eq.(2-65)

$$\tilde{U}_{st}(t_x,\Theta) = \frac{j\exp(jt_y l_0)}{2t_y}\tilde{F}[(\underline{T}-k_0\underline{s}_0)Q^{-1}] \tag{3-29}$$

Imagining that in Fig.(3-5) the plane wave is insonified in an opposite direction, the signal received on the line $y_1 = l_0$ will be reflection signal. Then, it is easy to show that the diffraction-projection formula for the reflection signal will has the form

$$\tilde{U}_{sr}(t_x,\Theta) = \frac{j\exp(jt_y l_0)}{2t_y}\tilde{F}[(\underline{T}+k_0\underline{s}_0)Q^{-1}] \tag{3-30}$$

where $\tilde{U}_{st}(t_x,\Theta)$ and $\tilde{U}_{sr}(t_x,\Theta)$ represent the Fourier transform of the transmission and the reflection signals respectively; $\tilde{F}[(\underline{T}-k_0\underline{s}_0)Q^{-1}]$ and $\tilde{F}[(\underline{T}+k_0\underline{s}_0)Q^{-1}]$ are the Fourier transform of the object function evaluated on the curvilinear coordinates $\{(\underline{T}-k_0\underline{s}_0)Q^{-1};\ \underline{T} = (t_x,t_y),\ t_y = \sqrt{k_0^2-t_x^2},\ |t_x|<k_0\}$ and $\{(\underline{T}+k_0\underline{s}_0)Q^{-1};\ \underline{T} = (t_x,t_y),\ t_y = \sqrt{k_0^2-t_x^2},\ |t_x|<k_0\}$ respectively.

Assume that $\underline{W} = (u,v)$ represents the position vector on the rectangular coordinates u-v in the spatial Fourier domain of the object function. From the vector equations $\underline{W} = (\underline{T}-k_0\underline{s}_0)Q^{-1}$ and $\underline{W} = (\underline{T}+k_0\underline{s}_0)Q^{-1}$, two relationships between a point (u,v) on the rectangular coordinates and a point (t_x,Θ) on the curvilinear coordinates can be found

$$\begin{cases} u = t_x\sin\Theta+(t_y-k_0)\cos\Theta \\ v = -t_x\cos\Theta+(t_y-k_0)\sin\Theta \end{cases} \tag{3-31}$$

and

$$\begin{cases} u = t_x\sin\Theta+(t_y+k_0)\cos\Theta \\ v = -t_x\cos\Theta+(t_y+k_0)\sin\Theta \end{cases} \tag{3-32}$$

Next, we will derive the relationships between a point (t_x,Θ) on the curvilinear coordinates and a point (u,v) on the rectangular coordinates from Eq.(3-31) and Eq.(3-32).

Fig.(3-6)(a) and (b) show the relations among the vectors $\underline{W}$, $\underline{T}$ and $k_0\underline{s}_0$ for the transmission and the reflection signals respectively. α is the angle between the vectors $\underline{W}$ and $\underline{W}-\underline{T}$, and β represents the angle between the vector $\underline{W}$ and the positive direction of the u axis.

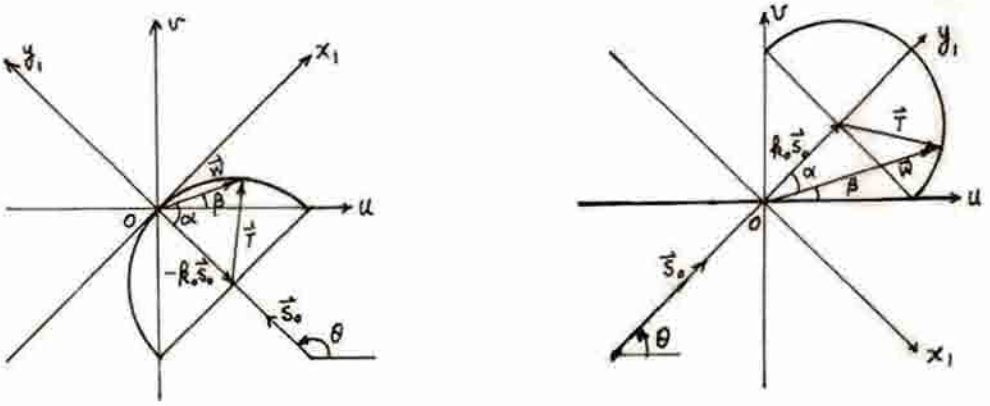

(a) (b)

Fig.(3-6) The relations among the vectors $\underline{W}$, $\underline{T}$ and $k_0\underline{s}_0$ (a) for the transmission signals (b) for the reflection signals

From Eq.(3-31), one obtains

$$u^2+v^2 = t_x^2+(t_y-k_0)^2 = t_x^2+k_\delta^2-t_x^2+k_\delta^2-2k_0t_y = 2k_\delta^2-2k_0t_y \tag{3-33}$$

From the equation above, one can solve t_x

$$t_x = \sqrt{k_\delta^2-\left(\frac{2k_\delta^2-u^2-v^2}{2k_0}\right)^2} \tag{3-34}$$

From the Fig.(3-6)(a), the relationship among the angles θ, α and β is clear

$$\theta = \pi-(\alpha-\beta) \tag{3-35}$$

where

$$\alpha = \cos^{-1}\left(\frac{\sqrt{u^2+v^2}}{2k_0}\right) \tag{3-36}$$

$$\beta = t_g^{-1}\left(\frac{v}{u}\right) \tag{3-37}$$

Similarly, from Eq.(3-32), we obtain

$$u^2+v^2 = 2k_\delta^2+2k_0t_y \tag{3-38}$$

Solving t_x from the above equation, one finds that the expression for t_x is the same as that in Eq.(3-34)

$$t_x = \sqrt{k_\delta^2-\left(\frac{2k_\delta^2-u^2-v^2}{2k_0}\right)^2} \tag{3-39}$$

From Fig.(3-6)(b), another relationship among θ, α and β can be shown

$$\theta = \alpha+\beta \tag{3-40}$$

Combining Eq.(3-34), Eq.(3-35), Eq.(3-39) and Eq.(3-40), one obtains the group of the relationships between a point (t_x,θ) on the curvilinear coordinates and

a point (u,v) on the rectangular coordinates for the transmission and the reflection signals respectively

$$\begin{cases} t_x = \sqrt{k_\delta^2 - \left(\dfrac{2k_\delta - u^2 - v^2}{2k_0}\right)^2} \\ \Theta = n + t_g^{-1}\left(\dfrac{v}{u}\right) - \cos^{-1}\left(\dfrac{\sqrt{u^2+v^2}}{2k_0}\right) \end{cases} \tag{3-41}$$

and

$$\begin{cases} t_x = \sqrt{k_\delta^2 - \left(\dfrac{2k_\delta - u^2 - v^2}{2k_0}\right)^2} \\ \Theta = t_g^{-1}\left(\dfrac{v}{u}\right) + \cos^{-1}\left(\dfrac{\sqrt{u^2+v^2}}{2k_0}\right) \end{cases} \tag{3-42}$$

(2) Image reconstruction

From Eq.(3-29) and Eq.(3-30), one will obtain the Fourier-domain coverages of the object function for the TRDCT (see Fig.(3-7)).

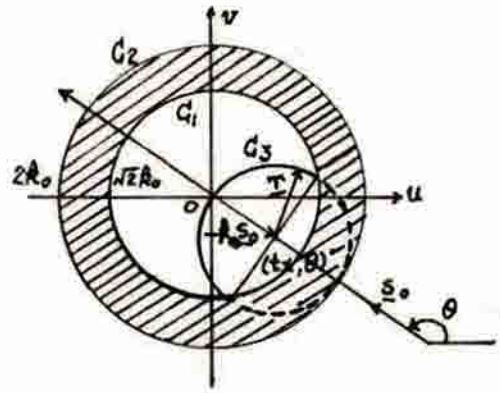

Fig.(3-7) Fourier-domain coverages of the TRDCT

In this figure, the circle C_3 is formed by the track of the point (u,v) on the Fourier-domain rectangular coordinates when t_x varies from $-k_0$ to $+k_0$ with Θ fixed for $\Theta = \Theta'$ and $\Theta = \Theta'+\pi$ respectively. The real half and the dashed half of the circle are corresponding to Eq.(3-31) and Eq.(3-32) respectively. The interior area of the circle C_2 which is centered on the origin of the coordinates and with a radius of $2k_0$ is covered by the diffracted data as Θ varies from 0° to 360° (the interior area of the circle C_1 is covered by the transmission data, and the ring area between the circles C_1 and C_2 is covered by the reflection data). From Fig.(3-7) it is seen that as the TRDCT can provide more high-frequency information of the object function than the conventional diffraction tomography, it is preferable that the TRDCT will give a higher-resolution image reconstruction.

To reconstruct the images using the IFFT, it is required to calculate the Fourier transform of the object function on the rectangular grids of the rectangular coordinates from the Fourier transform of the object function on the curvilinear coordinates, $F[(T \pm k_0 s_0)\Theta^{-1}]$, using some interpolation scheme.

Here, the commonly used bilinear interpolation technique is employed[91]

$$\tilde{U}_s(t_x;\Theta) = \sum_{i=1}^{N_{tx}-1} \sum_{j=1}^{N_\theta-1} \tilde{U}_s(t_{xi};\Theta_j)h_1(t_x-t_{xi})h_2(\Theta-\Theta_j) \qquad (3\text{-}43)$$

where

$$h_1(t_x-t_{xi}) = \begin{cases} 1-\dfrac{|t_x-t_{xi}|}{\Delta t_x}; & |t_x-t_{xi}| \leqslant \Delta t_x \\ 0 & ;\ \text{otherwise} \end{cases} \qquad (3\text{-}44)$$

$$h_2(\Theta-\Theta_j) = \begin{cases} 1-\dfrac{|\Theta-\Theta_j|}{\Delta\Theta}; & |\Theta-\Theta_j| \leqslant \Delta\Theta \\ 0 & ;\ \text{otherwise} \end{cases} \qquad (3\text{-}45)$$

where both t_x and Θ are constant; $\tilde{U}_s(t_{xi},\Theta_j)$ represents the discrete Fourier transform of the measured scattered field on the rectangular grids (t_{xi},Θ_j) of the curvilinear coordinates; $\tilde{U}_s(t_x,\Theta)$ is the Fourier transform of the scattered field evaluated on the point (t_x,Θ) of the curvilinear coordinates and is corresponding to the rectangular grid point (u,v) of the rectangular coordinates. N_{tx} and N_θ are the numbers of the discrete points of t_x and Θ respectively. The procedure of the bilinear interpolation is described in the following: first, the point (t_x,Θ), which is corresponding to the rectangular grid point (u,v) of the rectangular coordinates, of the curvilinear coordinates will be found according to Eq.(3-41) or Eq.(3-42), then the Fourier transform of the scattered field on the point (t_x,Θ) will be calculated by Eq.(3-43). After multiplying by a function factor shown in Eq.(3-29) or Eq.(3-30), the Fourier transform of the scattered field on the point (t_x,Θ) is assigned to the corresponding rectangular grid point (u,v) of the rectangular coordinates (if the point (u,v) belongs to the ring area between the circles C_1 and C_2 shown in Fig.(3-7), the point (t_x,Θ) is calculated using Eq.(3-42); and if it belongs to the interior area of the circle C_1, (t_x,Θ) is calculated using Eq.(3-41)).

In order to diminish the Gibbs oscillation phenomenon in the reconstructed images, Blackman window[106] is is applied to the Fourier transform of the object function on the rectangular grid points of the rectangular coordinates. The Blackman window is defined by

$$b(\underline{W}) = \begin{cases} 0.42-0.5\cos\dfrac{2\pi r}{4k_0}+0.08\cos\dfrac{4\pi r}{4k_0}; & |\underline{W}| \leqslant 2k_0 \\ 0 & ;\ |\underline{W}| > 2k_0 \end{cases} \qquad (3\text{-}46)$$

where

$$r = \sqrt{u^2+v^2}+2k_0 \qquad (3\text{-}47)$$

Taking the two-dimensional IFFT of the windowed Fourier transform $F(\underline{W})b(\underline{W})$, one will reconstruct the image of the object function.

It should be noticed that although the higher-frequency information of the object function is used in the TRDCT and hence the higher resolution images will be reconstructed, the high-frequency noise is accompanied with the image reconstructions of the TRDCT. In order to solve the high-frequency noise

problem, nonlinear-smoothing image processing technique[37] is adopted. By properly choosing smoothing weights and threshold in the nonlinear-smoothing process, not only the high-frequency resolution of the TRDCT is kept, but the high-frequency noise in the processed images is mostly excluded. The nonlinear-smoothing image processing technique is described briefly in the following:

Suppose a pixel in the reconstructed image is V_1, and eight pixels which surround V_1 is V_2 to V_9 and is arranged as follows

$$\begin{matrix} V_6 & V_2 & V_7 \\ V_3 & V_1 & V_4 \\ V_8 & V_5 & V_9 \end{matrix}$$

After the nonlinear-smoothing processing, the density of the pixel V_1 becomes

$$\frac{W_1 V_1 + W_2 \sum_{i=2}^{5} f_i V_i + W_3 \sum_{i=6}^{9} f_i V_i}{W_1 + W_2 \sum_{i=2}^{5} f_i + W_3 \sum_{i=6}^{9} f_i} \qquad (3\text{-}48)$$

where

$$f_i = \begin{cases} 1; & |V_i - V_1| \leq t \\ 0; & \text{otherwise} \end{cases} \qquad (3\text{-}49)$$

where W_1, W_2 and W_3 are smoothing weights, and t is the threshold (these quantities are all non-negative and are determined by experiments). If V_i is a boundary point, for some values of i, V_i will be undefined. In this case, we simply set $f_i = 0$.

(3) Computer simulations

Fig.(3-8)(a) is the 128x128 pixel image reconstructed by using the Fourier-domain bilinear interpolation algorithm of the conventional transmission diffraction tomography from the 64x128 diffracted data. Fig.(3-9)(a) is the 128x128 pixel image reconstructed by using the Fourier-domain bilinear interpolation reconstruction algorithm of the TRDCT from the 2(64x128) diffracted data. Fig.(3-10)(a) is obtained by the nonlinear-smoothing processing of Fig.(3-9)(a). It should be noticed that the physical dimension of the phantom used in the image reconstruction of Fig.(3-9)(a) is only $1/\sqrt{2}$ of that used in the image reconstruction of Fig.(3-8)(a) (the frequency sampling intervals for the image reconstructions of Fig.(3-8)(a) and Fig.(3-9)(a) are $\sqrt{2}k_0/128$ and $2k_0/128$, and the spatial sampling intervals are $\sqrt{2}\pi/k_0$ and π/k_0, respectively). Therefore, although the high-frequency resolution of Fig.(3-8)(a) looks almost the same as that of Fig.(3-9)(a), the high-frequency resolution of Fig.(3-9)(a), in actual, is much higher. From Fig.(3-10)(a), it is shown that the nonlinear-smoothing image processing diminishes the high-frequency artifacts in Fig.(3-9)(a) while keeps the higher high-frequency resolution of the TRDCT (here, the smoothing weights W_1, W_2 and W_3 are 9, 4 and 1, respectively, and the threshold is chosen as 0.05).

Fig.(3-8)(b) to Fig.(3-10)(b) are the comparisons of the reconstructed values (real line) and the real values (dashed line) on the line $y = -0.605$ (see Fig.(3-1)(b)) corresponding to Fig.(3-8)(a) to Fig.(3-10)(a),

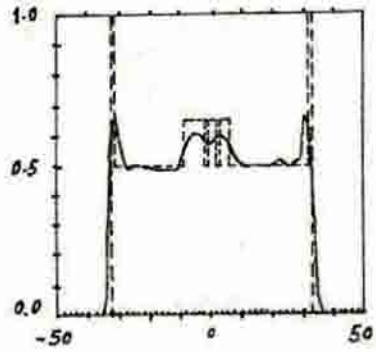

(a) (b)

Fig.(3-8) (a) 128x128 pixel image reconstructed by the conventional transmission diffraction tomography from the 64x128 diffracted data (b) The comparison of the reconstructed values (real line) and the real values (dashed line) on the line y = -0.605 (see Fig.(3-1)(b))

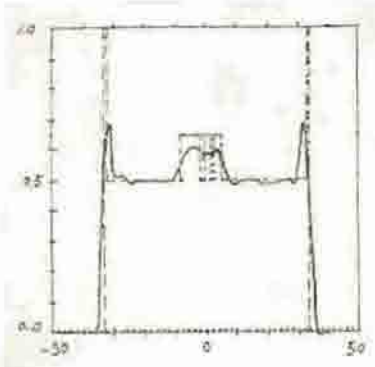

(a) (b)

Fig.(3-9) (a) 128x128 pixel image reconstructed by the TRDCT from the 64x128 diffracted data (b) The comparison of the reconstructed values (real line) and the real values (dashed line) on the line y = -0.605 (see Fig.(3-1)(b))

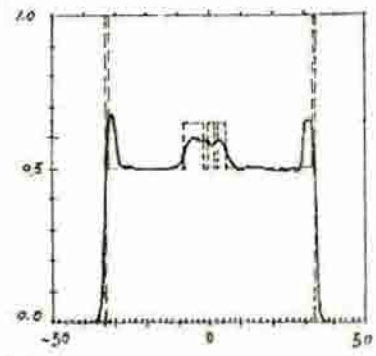

(a) (b)

Fig.(3-10) (a) 128x128 pixel image reconstructed by the TRDCT from the 64x128 diffracted data and then processed by the nonlinear-smoothing image processing technique (b) The comparison of the reconstructed values (real line) and the real values (dashed line) on the line y = -0.605 (see Fig.(3-1)(b))

respectively. Table (3-2) gives the comparisons of the "distances" of the reconstructed images. From the computer simulations above, it is observed that

the images reconstructed by the TRDCT and then processed by the nonlinear-smoothing image processing technique are not only of higher resolution, but of higher quality when they are evaluated by the image quality criteria of this paper.

Table(3-2) The comparisons of the "distances" of the reconstructed images

Figure	Specifications	d_1	r_1	e_1	d_2	r_2	e_2	max	min
(3-8)	Transmission CT	.29	.12	.41	.29	.12	.41	.94	$-.31\times10^{-1}$
(3-9)	TRDCT	.29	.12	.40	.29	.12	.40	.98	$-.27\times10^{-1}$
(3-10)	TRDCT & smoothing	.29	.11	.40	.29	.11	.40	.98	$-.17\times10^{-1}$

3. Fourier-Domain Interpolation Reconstruction Algorithm for Synthetic Aperture Diffraction Tomography

(1) Basic principle

The datum acquisition geometry of the SADCT is shown in Fig.(3-11). Where the x-y coordinates are fixed in the space; L_t and L_r are the transmitting and the receiving lines along which the transmitter and the receiver can be moved respectively; these two lines are parallel and d is the distance between them; $F(\underline{r})$ represents the two-dimensional object function of the object located between L_t and L_r and centered at the point (0,d/2); s represents a cross-section of the object to be imaged.

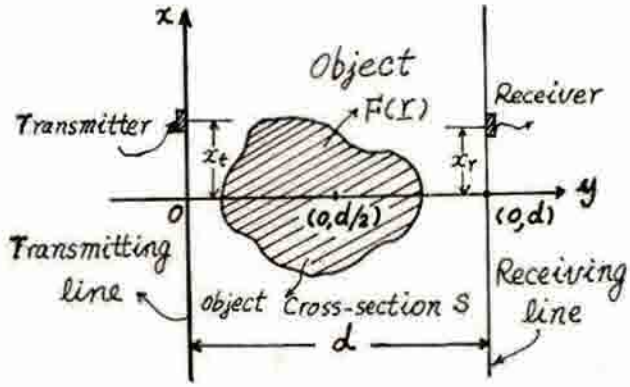

Fig.(3-11) Datum acquisition geometry of the SADCT

The transmitting and the receiving transducers in Fig.(3-11) are immersed in the echoless water tanker and their coordinates on L_t and L_r are indicated by x_t and x_r, respectively. For each fixed position of the transmitter, the receiver can be moved to N positions along L_r. Therefore, if the transmitter is moved to N positions along L_t, NxN diffracted data can be obtained. If the measuring system is rotated around the object for 90° (or the measuring system is fixed, the object is rotated 90° around its center in an opposite direction) and the datum acquisition procedure above is repeated, another NxN diffracted data can be obtained. From these two sets of diffracted data, images of the object function can be reconstructed.

In what follows, the diffraction-projection formulas for the SADCT[89] will be found from the datum acquisition geometry shown in Fig.(3-11) and from

the integral solution Eq.(2-47) of the scattered field. Assume that the incident and the scattered field on a space point $\underline{r} = (x,y)$ produced by the transmitter located at the point $(x_t,0)$ on L_t are $U_i(\underline{r};x_t)$ and $U_s(\underline{r};x_t)$ respectively. According to the angular spectrum expansion[107], the integral expression of the incident field $U_i(\underline{r};0)$ on the space point $\underline{r}$ when the transmitter is located at the origin of the coordinates can be determined. For $\underline{r} = (x,0)$, the incident field $U_i(\underline{r};0)$ will be notated as $U_i(x,0;0)$, and it will represent the field on L_t when the source is located at the origin of the coordinates. Taking the Fourier transform of $U_i(x,0;0)$ with respect to the variable x, and notating the result as $A_t(k_x;0)$, There will be

$$A_t(k_x) = \int_{-\infty}^{+\infty} u_i(x,0;0)\exp(-jk_x x)dx \tag{3-50}$$

Taking the Fourier transform of $U_i(\underline{r};0)$ with respect to the variable x and leaving the variable y as a parameter, one shows that

$$A_t(k_x;y;0) = \int_{-\infty}^{+\infty} u_i(\underline{r};0)\exp(-jk_x x)dx \tag{3-51}$$

Thus, $U_i(\underline{r};0)$ can be expressed as a Fourier integration of $A_t(k_x;y;0)$

$$u_i(\underline{r};0) = \frac{1}{2\pi}\int_{-\infty}^{+\infty} A_t(k_x;y;0)\exp(jk_x x)dk_x \tag{3-52}$$

In the source-free area, the incident field $U_i(\underline{r};0)$ satisfies the following Helmholtz equation

$$\nabla^2 U_i(\underline{r};0)+k_0^2 U_i(\underline{r};0) = 0 \tag{3-53}$$

From the equation above, the boundary-value problem of $A_t(k_x;y;0)$ can be formed

$$\begin{cases} \dfrac{d^2 A_t(k_x;y;0)}{dy^2}+(k_0^2-k_x^2)A_t(k_x;y;0) = 0 \\ A_t(k_x;y;0)\big|_{y=0} = A_t(k_x;0) \end{cases} \tag{3-54}$$

Solving Eq.(3-54), we have

$$A_t(k_x;y;0) = A_t(k_x;0)\exp(jk_y y) \tag{3-55}$$

where

$$k_y = \sqrt{k_0^2-k_x^2} \tag{3-56}$$

Substituting Eq.(3-55) into Eq.(3-52), one finds

$$u_i(\underline{r};0) = \frac{1}{2\pi}\int_{-\infty}^{+\infty} A_t(k_x;0)\exp(j\underline{K}\cdot\underline{r})dk_x \tag{3-57}$$

where the vector $\underline{K} = (k_x,k_y)$.

If the transmitter is located at a point $(x_t;0)$ on the transmitting line

L_t, Eq.(3-50) can be changed accordingly to

$$A_t(k_x;x_t) = \int_{-\infty}^{+\infty} u_i(x,0;x_t)\exp(-jk_x x)dx \tag{3-58}$$

As $U_i(x,0;x_t) = U_i(x-x_t,0;0)$, from the equation above one can find that

$$A_t(k_x;x_t) = A_t(k_x;0)\exp(-jk_x x_t) \tag{3-59}$$

Then, using Eq.(3-57), the integral expression of the incident field on a space point $\underline{r}$ when the transmitter is located at the point $(x_t,0)$ on L_t can be obtained

$$u_i(\underline{r};x_t) = \frac{1}{2\pi}\int_{-\infty}^{+\infty} A_t(k_x)\exp(-jk_x x_t)\exp(j\underline{K}\cdot\underline{r})dk_x \tag{3-60}$$

where $A_t(k_x)$ stands for $A_t(k_x;0)$.

Substituting Eq.(2-45) into Eq.(2-44), one can obtain the integral expression of the Green's function in the two-dimensional free-space. Renaming the integral variable K_x to t_x and then substituting both the integral expression and Eq.(3-60) into Eq.(2-47), the scattered field on a point (x_r,d) on the receiving line L_t when the transmitter is located at the point $(x_t,0)$ can be obtained

$$u_s(x_r;x_t) = \frac{1}{(2\pi)^2}\int_{-\infty}^{+\infty}\int_{-\infty}^{+\infty}\frac{j\exp(jt_y d)}{2t_y}A_t(k_x)$$

$$\cdot\{j_s F(\underline{r}_0)\exp[-j(\underline{T}-\underline{K})\cdot\underline{r}_0]d\underline{r}_0\}\exp[j(t_x x_r - k_x x_t)dt_x dk_x \tag{3-61}$$

where $\underline{T} = (t_x,t_y)$, and

$$t_y = \sqrt{k_0^2 - t_x^2} \tag{3-62}$$

Taking the two-dimensional Fourier transform of $U_s(x_r;-x_t)$, we obtain

$$\widetilde{U}_s(t_x;k_x) = \frac{j\exp(jt_y d)}{2t_y}A_t(k_x)\int_s F(\underline{r}_0)\exp[-j(\underline{T}-\underline{K})\cdot\underline{r}_0]d\underline{r}_0 \tag{3-63}$$

Taking into account the spatial filter characteristics of the aperture size of the receiver for the scattered field, $A_r(t_x)$, the Eq.(3-63) can be slightly modified to

$$\widetilde{P}_{s\,a}(t_x;k_x) = \frac{j\exp(jt_y d)}{2t_y}A_r(t_x)A_t(k_x)\int_s F(\underline{r}_0)\exp[-j(\underline{T}-\underline{K})\cdot\underline{r}_0]d\underline{r}_0 \tag{3-64}$$

where $\widetilde{P}_{s\,a}(t_x;k_x)$ is the Fourier transform of the received scattered field. From the above equation, the diffraction-projection formula for the SADCT is obtained

$$\widetilde{F}(\underline{T}-\underline{K}) = -\frac{2jt_y\exp(-jt_y d)}{A_r(t_x)A_t(k_x)}\widetilde{P}_{s\,a}(t_x;k_x) \tag{3-65}$$

where

$$\tilde{F}(\underline{T}-\underline{K}) = \int_s F(\underline{r}_0)\exp[-j(\underline{T}-\underline{K})\cdot\underline{r}_0]d\underline{r}_0 \tag{3-66}$$

is the Fourier transform of the object function on the curvilinear coordinates $[\underline{T}-\underline{K};\ |t_x|\leqslant k_0,\ |k_x|\leqslant k_0)$.

To make the Fourier domain of the object function covered sufficiently by the diffracted data, it is necessary to rotate the object around its center for 90°. Similarly, the diffraction-projection formula for the 90° rotated object can be found

$$\tilde{F}[(\underline{T}-\underline{K})Q] = -\frac{2jt_y\exp(-jt_yd)}{A_r(t_x)A_t(k_x)}\tilde{P}_{sb}(t_x;k_x) \tag{3-67}$$

where $\tilde{F}[(\underline{T}-\underline{K})Q]$ is the Fourier transform of the object function on the curvilinear coordinates $[(\underline{T}-\underline{K})Q;\ |t_x|\leqslant k_0$ and $|k_x|\leqslant k_0]$ after the 90° rotation of the object; $\tilde{P}_{sb}(t_x;k_x)$ is the Fourier transform of the measured scattered field after the rotation of the object; $\underline{T}$ and $\underline{K}$ are row vectors; Q is the same as that in Eq.(2-51) with $\Theta_i = 90°$.

Eq.(3-66) and Eq.(3-67) build up a group of the relationships between the Fourier transform of the measured scattered field and the Fourier transform of the object function on the curvilinear coordinates. From those relationships, images can be reconstructed.

(2) Fourier-domain interpolation reconstruction algorithm for the SADCT

Assume that $\underline{W} = (u,v)$ is a vector on the rectangular coordinates of the Fourier domain. From the vector equations $\underline{W} = \underline{T}-\underline{K}$ and $\underline{W} = (\underline{T}-\underline{K})Q$, one will obtain the relationships between a point (u,v) on the rectangular coordinates and a point (t_x,k_x) on the curvilinear coordinates

$$\begin{cases} u = t_x - k_x \\ v = t_y - k_y \end{cases} \tag{3-68}$$

$$\begin{cases} u = t_y - k_y \\ v = -t_x + k_x \end{cases} \tag{3-69}$$

where $|t_x|\leqslant k_0$ and $|k_x|\leqslant k_0$. If $|t_x|>k_0$ or $|k_x|>k_0$, the scattered field is actually an attenuated field. When the receiving line L_r is placed far enough from the object, the effects of the attenuated field are negligible. From Eq.(3-68) and Eq.(3-69), Fourier-domain coverage areas A (before the rotation of the object) and B (after the 90° rotation of the object) can be obtained[99], as is shown in Fig.(3-12).

In order to carry out the Fourier-domain interpolation, it is necessary to find a group of relationships between the curvilinear coordinates and the rectangular coordinates. From Eq.(3-56) and Eq.(3-62), it is shown that

$$t_x^2+t_y^2 = k_0^2 \tag{3-70}$$

$$k_x^2+k_y^2 = k_0^2 \tag{3-71}$$

and from Eq.(3-68), one has

$$(u-t_x)^2+(v-t_y)^2 = k_0^2 \tag{3-72}$$

$$(u+k_x)^2+(v+k_y)^2 = k_0^2 \tag{3-73}$$

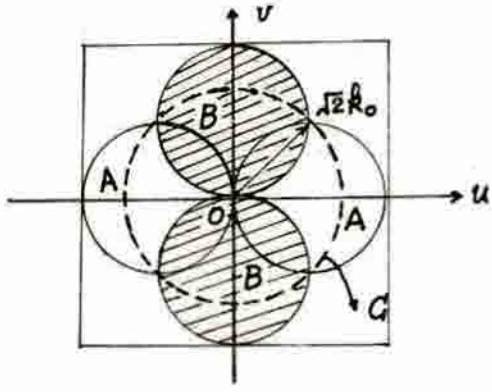

Fig.(3-12) Fourier-domain coverage areas A and B of the SADCT. The area A and the area B represent the coverages before and after the 90° rotation of the object respectively.

Eq.(3-72) represents a circle centered at (t_x, t_y) with a radius of k_0 on the Fourier-domain rectangular coordinates. From Eq.(3-70), it can be seen that the trace of the center (t_x, t_y) of the circle determined by Eq.(3-72) is also a circle with a radius of k_0, but with its center on the origin of the coordinates. For t_y is always greater than zero, the circle represented by Eq.(3-70) is the upper half circle, as is shown by the dashed line in Fig.(3-13). Similarly, Eq.(3-73) represents the circle centered at $(-k_x, -k_y)$ and with the radius of k_0 in the Fourier-domain rectangular coordinates, and the trace of the center $(-k_x, -k_y)$ of the circle forms the lower half circle in Fig.(3-13) which is centered at the origin of the coordinates with a radius of k_0. The Fourier-domain coverage area A in Fig.(3-12) is formed by the set of points (u,v) which satisfy the Eq.(3-72) and Eq.(3-73) simultaneously. From Eq.(3-72) and Eq.(3-73), t_x and k_x can be solved respectively in terms of a given point (u,v). Considering Fig.(3-13), one will obtain the relationship between a point (t_x, k_x) on the curvilinear coordinates and a point (u,v) on the rectangular coordinates in the different quarters of the rectangular coordinates of the Fourier-domain coverage area A.

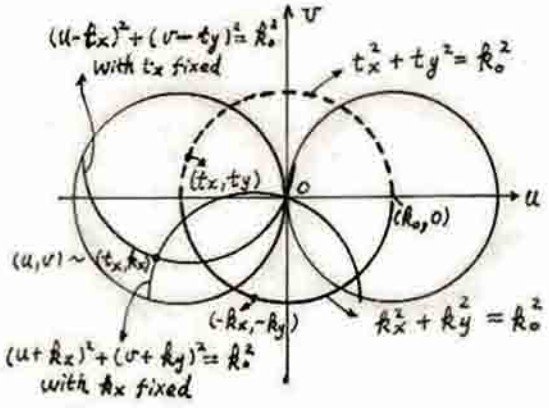

Fig.(3-13) Relationships between the curvilinear and the rectangular coordinates

If the point (u,v) is in the first or the third quarter, there will be

$$\begin{cases} t_x = \dfrac{1}{2}(u-q_1) \\ k_x = -\dfrac{1}{2}(u+q_1) \end{cases} \tag{3-74}$$

where

$$q_1 = |v| \cdot \sqrt{\frac{4k_0^2}{u^2+v^2} - 1} \tag{3-75}$$

If the point (u,v) is in the second or the fourth quarter, we will show that

$$\begin{cases} t_x = \dfrac{1}{2}(u+q_1) \\ k_x = -\dfrac{1}{2}(u-q_1) \end{cases} \tag{3-76}$$

From Eq.(3-69), we have

$$(u-t_y)^2+(v+t_x)^2 = k_0^2 \tag{3-77}$$

$$(u+k_y)^2+(v-k_x)^2 = k_0^2 \tag{3-78}$$

Similarly, the set of points (u,v) which satisfy Eq.(3-77) and Eq.(3-78) simultaneously will form the Fourier-domain coverage area B, as is shown in Fig.(3-12). In the same way, the relationship between the curvilinear and the rectangular coordinates, which is similar to what is shown in Fig.(3-13), can be obtained from Eq.(3-77) and Eq.(3-78). Then, the relationship between a point (t_x,k_x) on the curvilinear coordinates and a point (u,v) on the rectangular coordinates in the different quarters of the rectangular coordinates of the Fourier-domain coverage area B will be found. If the point (u,v) is in the first and the third quarter, it is easy to show that

$$\begin{cases} t_x = -\dfrac{1}{2}(v-q_2) \\ k_x = \dfrac{1}{2}(v+q_2) \end{cases} \tag{3-79}$$

where

$$q_2 = |u| \cdot \sqrt{\frac{4k_0^2}{u^2+v^2} - 1} \tag{3-80}$$

If the point (u,v) is in the second or the fourth quarter, we will obtain

$$
\begin{cases}
t_x = -\dfrac{1}{2}(v+q_2) \\
k_x = \dfrac{1}{2}(v-q_2)
\end{cases}
\tag{3-81}
$$

From Eq.(3-74), Eq.(3-76), Eq.(3-79) and Eq.(3-81), first, on the curvilinear coordinates, the positions of the rectangular grid points of the Fourier-domain rectangular coordinates can be determined; and then the Fourier transform of the object function on the rectangular grid points of the rectangular coordinates can be calculated using the Fourier-domain interpolation procedure, which is described as follows: given a rectangular grid point (u,v) of the rectangular coordinates, one should judge which of Fourier-domain coverage areas (A or B) this point belongs to. If it belongs to the area A, the corresponding point (t_x,k_x) on the curvilinear coordinates is determined by Eq.(3-74) or Eq.(3-76), and the Fourier transform of the object function on this point will be calculated from the known discrete diffracted data using some interpolation scheme and will be taken as the Fourier transform of the object function on the rectangular grid point (u,v) of the rectangular coordinates. If the point (u,v) belongs to the area B, the corresponding point (t_x,k_x) is found by Eq.(3-78) and Eq.(3-81), and similarly, the Fourier transform of the object function on the point (u,v) can be calculated using some interpolation scheme. If the point (u,v) belongs to the area $A \cap B$, the average of the interpolation results above is taken as the Fourier transform of the object function on the point (u,v). Because the distribution of the points on which the discrete diffracted data are known is very uneven in the Fourier-domain coverage areas A and B of the SADCT (it is the case for both the low- and the high-frequency portions and especially for the vicinity of the boundaries of the areas A and B), to improve the quality of the reconstructed images, special consideration must be taken for the interpolation of the points near the boundaries of the areas A and B. This will be demonstrated in detail later. Applying the Blackman Window in Eq.(3-46) to the Fourier transform of the object function on the rectangular grid points of the rectangular coordinates and taking the two-dimensional IFFT, the images of the object function will be reconstructed.

(3) Computer simulations

In the following computer simulations, the image reconstructions of the SADCT for both the Fourier-domain interpolation algorithm and the interpolation-free algorithm proposed by Dr. D. Nahamoo et al. are given, and the comparisons of these two algorithms are carried out.

Fig.(3-14)(a) is the 128x128 pixel image reconstructed from the 2(128x128) diffracted data using the Fourier-domain nearest-neighbor interpolation[91]. Fig.(3-15)(a) is the 128x128 pixel image reconstructed from the same set of diffracted data using the interpolation-free algorithm. Fig.(3-14)(b) and Fig.(3-15)(b) are the comparisons of the reconstructed values (real line) and the real values (dashed line) on the line $y = -0.605$ (see Fig.(3-1)(b)) corresponding to Fig.(3-14)(a) and Fig.(3-15)(a), respectively. Table (3-3) gives the comparisons of the "distances" of the images reconstructed by the interpolation and interpolation-free algorithm. In addition, the VAX-11/730 computer CPU processing time for the image reconstructions of Fig.(3-14)(a) and Fig.(3-15)(a) are 2.58 and 19.3 minutes respectively, i.e., the time for the reconstruction of Fig.(3-14)(a) is only about 13% of that of Fig.(3-15)(a). From the computer simulations, it is seen that for the SADCT, the interpolation algorithm is not only faster than the

interpolation-free algorithm, but superior in the quality of the image reconstructions.

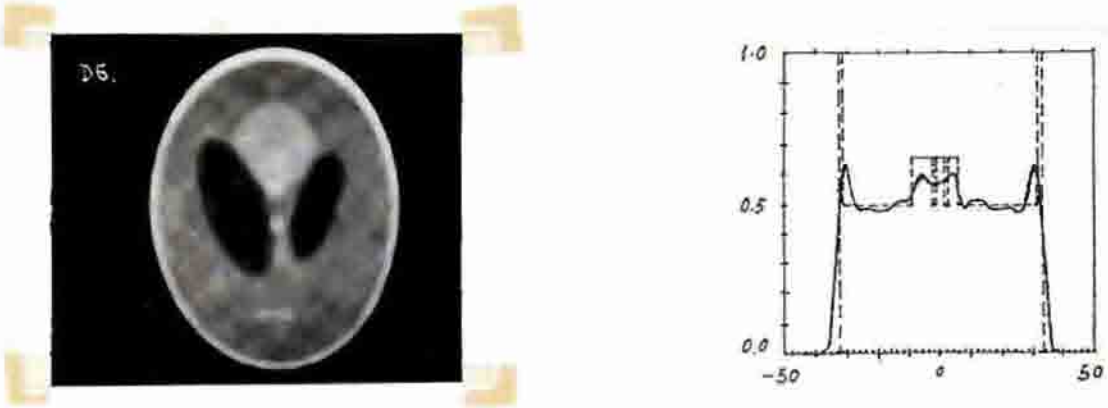

(a) (b)

Fig.(3-14) (a) 128x128 pixel image reconstructed by the interpolation algorithm of the SADCT from the 2(128x128) diffracted data (b) The comparison of the reconstructed values (real line) and the real values (dashed line) on the line y = -0.605 (see Fig.(3-1)(b))

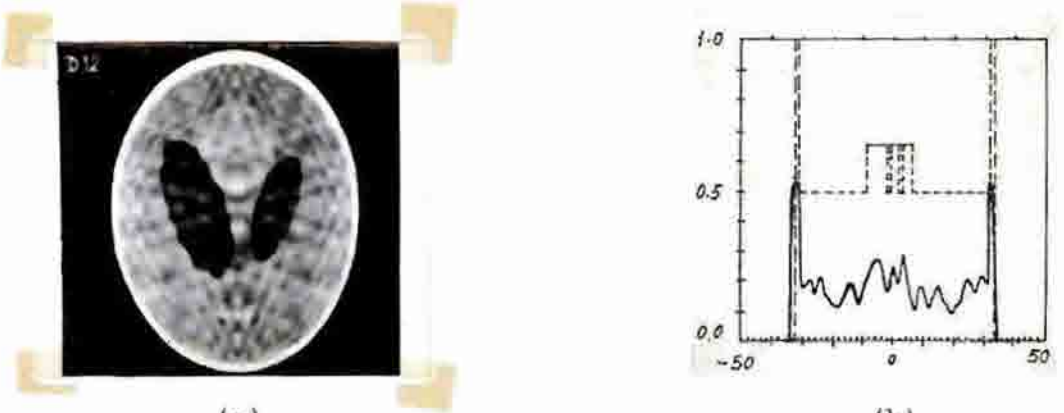

(a) (b)

Fig.(3-15) (a) 128x128 pixel image reconstructed by the interpolation-free algorithm of the SADCT from the the same set of diffracted data as those used in the reconstruction of Fig.(3-14) (a). (b) The comparison of the reconstructed values (real line) and the real values (dashed line) on the line y = -0.605 (see Fig.(3-1)(b))

Table(3-3) The comparisons of the "distances" of the images reconstructed by the interpolation and the interpolation-free algorithms

Figure	Specifications	d_1	r_1	e_1	d_2	r_2	e_2	max	min
(3-14)	Interpolation	.34	.16	.46	.34	.16	.46	.92	$-.50\times10^{-1}$
(3-15)	Interpolation-free	1.0	1.0	.84	.51	.42	.60	.77	-.41

With the coordinate system shown in Fig.(3-11), the center of the object is at (0,d/2). For the object function whose center is not at the origin of the coordinates contains a fast oscillating phase factor in its Fourier domain, which will cause inaccuracy in the Fourier-domain interpolation, higher quality images will be reconstructed if the center of the object is shifted back to the origin of the coordinates before the Fourier-domain

interpolation. Fig.(3-16)(a) is the same as Fig.(3-14)(a) except that the center of the object is shifted back to the origin of the coordinates after the Fourier-domain interpolation. It is seen clearly that striking artifacts are shown in this figure. Fig.(3-16)(b) is corresponding to Fig.(3-16)(a) and is the comparison of the reconstructed values (real line) and the real values (dashed line) on the line y = -0.605 (see Fig.(3-1)(b)). Table (3-4) is the comparison of the "distances" of Fig.(3-16)(a) and Fig.(3-14)(a). All the results above show that the quality of Fig.(3-16)(a) is lower than that of Fig.(3-14)(a).

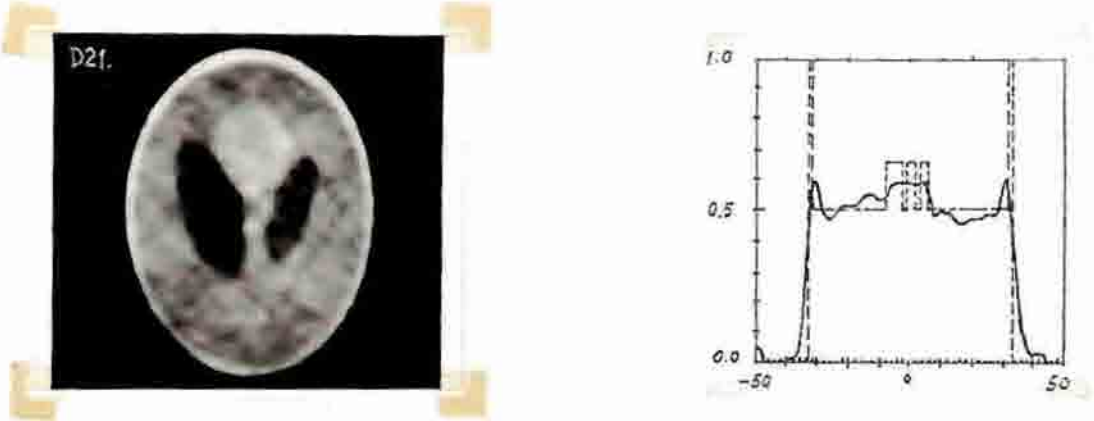

(a) (b)

Fig.(3-16) (a) 128x128 pixel image reconstructed with the same conditions as those for Fig.(3-14)(a), except that the center of the object is shifted back to the origin of the coordinates after the Fourier-domain interpolation (b) The comparison of the reconstructed values (real line) and the real values (dashed line) on the line y = -0.605 (see Fig.(3-1)(b))

Table(3-4) The comparisons of the "distances" of the images reconstructed with the center of the object shifted back to the origin of the coordinates before and after the Fourier-domain interpolation

Figure	Specifications	d_1	r_1	e_1	d_2	r_2	e_2	max	min
(3-14)	Shift before int.	.34	.16	.46	.34	.16	.46	.92	$-.50\times10^{-1}$
(3-16)	Shift after int.	.36	.20	.51	.36	.20	.51	.98	$-.95\times10^{-1}$

Fig.(3-17) shows the distribution of the rectangular grid points of the curvilinear coordinates on the rectangular coordinates in the Fourier-domain coverage area A (such distribution in the area B can be obtained by rotating Fig.(3-17) 90°). It is seen clearly from this figure that the known points of the Fourier transform of the object function are distributed densely near the u-axis, the center symmetric axis of the area A, while they are distributed sparsely near the boundaries (here, only the interior area of the circle centered at the origin with a radius of $\sqrt{2}k_0$ is considered). Therefore, the interpolation for the Fourier transform of the object function on the rectangular grid points of the rectangular coordinates near the boundaries of the area A using Eq.(3-74) and Eq.(3-76) will result in big error. However, those points which are near the boundaries of the area A are near the center symmetric axis (v-axis) of the area B. Hence, better results will be obtained if Eq.(3-74) and Eq.(3-76) are replaced by Eq.(3-79) and Eq.(3-81) for the interpolation of the points near the boundaries of the area A, and Eq.(3-79) and Eq.(3-81) are replaced by Eq.(3-74) and Eq.(3-76) for the interpolation of the points near the boundaries of the area B. In this paper, by the experiments, those points which satisfy the conditions $|t_x| \geq 31k_0/32$ or

$|k_x| \geq 31k_0/32$ are taken as the boundary points of the areas A and B. The above statements can be verified by the following computer simulations. Fig.(3-18)(a) is the same as Fig.(3-14)(a), but with no special consideration of the uneven nature of the distributions of the points near the boundaries of the Fourier-domain coverage areas A and B, and thus its quality is poor. Fig.(3-18)(b) is corresponding to Fig.(3-18)(a) and is the comparison of the reconstructed values (real line) and the real values (dashed line) on the line $y = -0.605$ (see Fig.(3-1)(b)). Table (3-5) shows the comparison of the "distance" of Fig.(3-18)(a) and Fig.(3-14)(a). All the results above illustrate that the quality of Fig.(3-18)(a) is lowered.

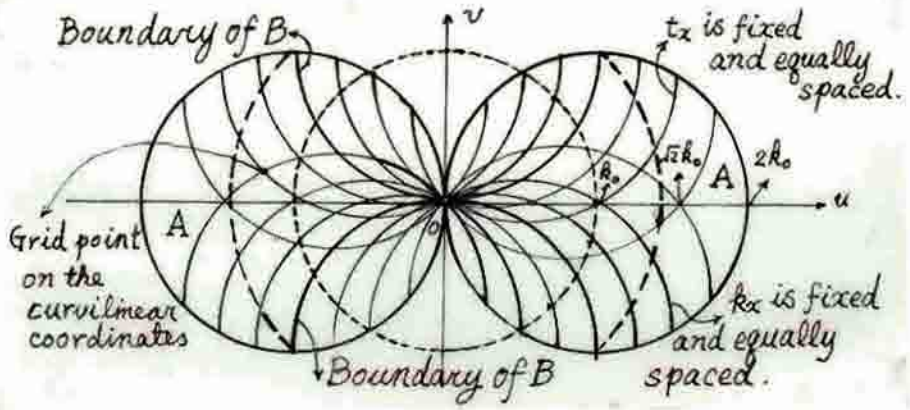

Fig.(3-17) The distribution of the rectangular grid points of the curvilinear coordinates on the rectangular coordinates in the Fourier-domain coverage area A

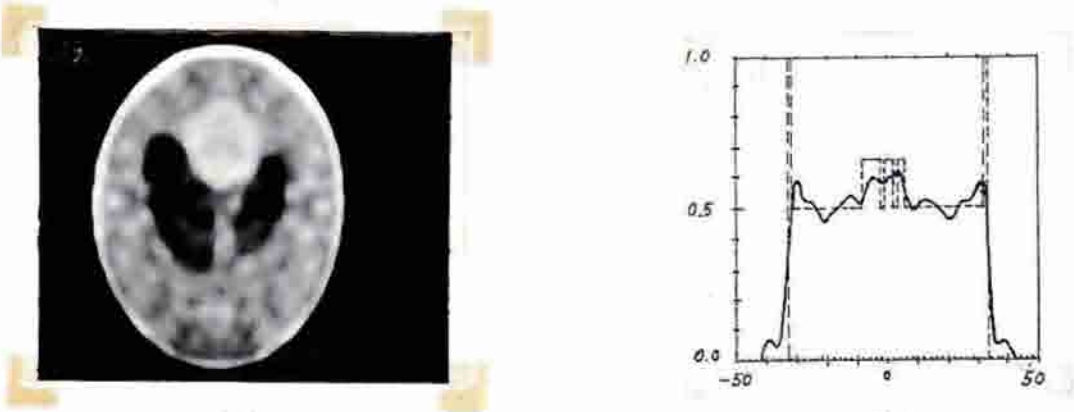

(a) (b)

Fig.(3-18) (a) 128x128 pixel image reconstructed with the same conditions as those for Fig.(3-14)(a), but with no special consideration for the interpolation of the points near the boundaries of the Fourier-domain coverage areas A and B (b) The comparison of the reconstructed values (real line) and the real values (dashed line) on the line $y = -0.605$ (see Fig.(3-1)(b))

Table(3-5) The comparisons of the "distances" of the images reconstructed with and without special consideration of the interpolation of the points near the boundaries of the Fourier-domain coverage areas A and B

Figure	Specifications	d_1	r_1	e_1	d_2	r_2	e_2	max	min
(3-14)	With special con.	.34	.16	.46	.34	.16	.46	.92	$-.50\times10^{-1}$
(3-18)	Without special con.	.37	.22	.54	.37	.21	.54	.91	-.11

IV. A NEW QUANTITATIVE REFLECTION IMAGING METHOD

1. Theoretical Preliminaries

Fig.(4-1) is the datum acquisition geometry of the QRI method. Where the x-y coordinates are fixed in the space; $F(\underline{r})$ represents the object function (Assume that the object is two-dimensional, and is immersed in the echoless water tanker and is placed within the focal zone of the ultrasonic field of the transducer); L represents the effective half-width of the focused ultrasonic beam; x' is the distance between the center of the beam and the y' axis; l_0 is the distance from the surface of the transducer to x axis. The transducer used in this paper is a transducer array consisted of many elementary transducers, which is used for both the transmitting and the receiving of the ultrasonic field. This transducer array is focused electrically and can be linearly scanned in a cross-section of the object along x axis. The focal zone of the ultrasonic field is the area formed by linearly scanning the segment of the ultrasonic beam centered at the focal point and stretched along the ultrasonic beam. Besides, the ultrasonic beam within the focal zone must be so narrow and even that it can be looked as plane wave approximately in the effective width 2L of each ultrasonic beam.

$$U_i(\underline{r};k_0) = \begin{cases} A\exp(jk_0\underline{s}_0\cdot\underline{r}); & |x-x'|\leqslant L \\ 0 ; & |x-x'|>L \end{cases} \tag{4-1}$$

where A is a complex constant, which represents the initial amplitude and the phase of the incident wave; $\underline{s}_0$ represents the unit vector in the direction of the plane wave insonification; $\underline{r} = (x,y)$ is the position vector in the space.

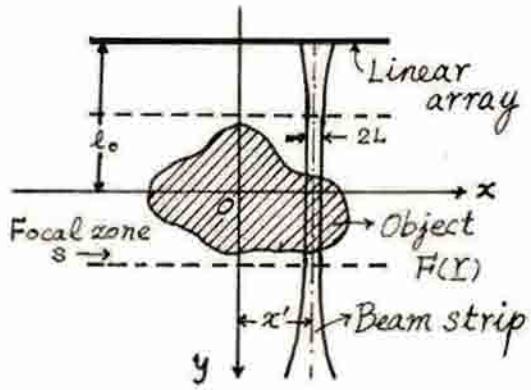

Datum acquisition geometry of the QRI method

If the transducer is placed so far from the object that the argument of the Hankel function in Eq.(2-45) is much greater than unity, i.e., $k_0|\underline{r}-\underline{r}_0|>1$, the expression of the two-dimensional free-space Green's function in Eq.(2-44) can be simplified to

$$g(\underline{r}|\underline{r}_0) = \frac{j}{4}\sqrt{\frac{2}{\pi k_0|\underline{r}-\underline{r}_0|}}\exp[j(k_0|\underline{r}-\underline{r}_0|-\frac{\pi}{4})] \tag{4-2}$$

Substituting both Eq.(4-1) and Eq.(4-2) into Eq.(2-47), one obtains

$$U_s(\underline{r};k_0) = \int_s F(\underline{r}_0)A\exp(jk_0\underline{s}_0\cdot\underline{r}_0)$$

$$\cdot\frac{j}{4}\sqrt{\frac{2}{\pi k_0|\underline{r}-\underline{r}_0|}}\exp[j(k_0|\underline{r}-\underline{r}_0|-\frac{\pi}{4})]d\underline{r}_0 \qquad (4-3)$$

where s represents the focal zone of the transducer array; k_0 in $U_s(\underline{r};k_0)$ emphasizes the frequency-dependent nature of the scattered field. If the center of the group of the elementary transducers is at the point $\underline{r} = (x',-l_0)$, Eq.(4-3) becomes

$$U_s(x',-l_0;k_0) = \int_{-\infty}^{+\infty}\int_{-\infty}^{+\infty} F(x_0,y_0)A\exp(jk_0y_0)$$

$$\cdot\frac{j}{4}\sqrt{\frac{2}{\pi k_0\sqrt{(x'-x_0)^2+(y-y_0)^2}}}\exp[j(k_0\sqrt{(x'-x_0)^2+(y-y_0)^2}-\pi/4)]dx_0dy_0 \qquad (4-4)$$

Considering the expression of the incident field, Eq.(4-1), Eq.(4-4) can be written as

$$U_s(x',-l_0;k_0) = \int_{-\infty}^{+\infty} A\exp(jk_0y_0)\cdot(j/4)[\int_{x'-L}^{x'+L} F(x_0,y_0)$$

$$\cdot\sqrt{\frac{2}{\pi k_0\sqrt{(x'-x_0)^2+(-l_0-y_0)^2}}}\exp[j(k_0\sqrt{(x'-x_0)^2+(-l_0-y_0)^2}-\pi/4)]dx_0\}dy_0 \qquad (4-5)$$

Suppose the ultrasonic beam is finely focused, the effective width 2L of the beam in the focal zone will be very small, and the variation of F(x,y) within the width 2L which is centered on the line x = x' will be negligible, and the following condition will be held

$$|-l_0-y_0| >> \max_{x'-L\leq x_0\leq x'+L}|x'-x_0| = L \qquad (4-6)$$

In this case, the integrand of the integration with respective to x_0 in Eq.(4-5) can be approximately looked as independent of the integral variable x_0 and can be taken out of the integral sign. Then, Eq.(4-5) can be further simplified

$$U_s(x',-l_0;k_0) = \int_{-\infty}^{+\infty} F(y_0)\cdot A'\exp(jk_0y_0)$$

$$\cdot\frac{j}{4}\sqrt{\frac{2}{\pi k_0|-l_0-y_0|}}\exp[j(k_0|-l_0-y_0|-\frac{\pi}{4})]dy_0 \qquad (4-7)$$

where A' = 2LA is a new constant; F(y) is the object function on the line x = x' and is given by

$$F(y) = \begin{cases} k_0^2[n^2(x',y)-1]; & (x',y)\in\text{object} \\ 0 \qquad\qquad ; & \text{otherwise} \end{cases} \qquad (4-8)$$

where $n(x',y) = C_0/C(x',y)$ is the distribution of the refractive index of the object on the line $x = x'$. For the convenience of the discussion, two new functions which are related to the distribution of the refractive index are introduced

$$n_1(y) = F(y)/k\delta \tag{4-9}$$

$$n_e(y) = n_1(y)/\sqrt{l_0+y} \tag{4-10}$$

where $n_1(y)$ is another form of the object function and is independent of the angular frequency ω; $n_e(y)$ is named as equivalent object function.

From Fig.(4-1), it is seen that l_0+y_0 is always greater than zero when the integral variable y_0 in Eq.(4-7) varies within the focal zone of the ultrasonic field. In this case, from Eq.(4-7), one will note that

$$\begin{aligned} U_s(x',-l_0;k_0) &= \int_{-\infty}^{+\infty} k\delta\, n_1(y_0)A'\exp(jk_0y_0) \\ &\quad \cdot \frac{j}{4}\sqrt{\frac{2}{\pi k_0(l_0+y_0)}}\exp(jk_0y_0)\exp[j(k_0l_0-(\pi/4))]dy_0 \\ &= \frac{jA'k\delta\exp[j(k_0l_0-\pi/4)]}{2\sqrt{2\pi k_0}}\tilde{n}_e(-2k_0) \end{aligned} \tag{4-11}$$

where $\tilde{n}_e(k)$ is the Fourier transform of $n_e(y)$

$$\tilde{n}_e(k) = \int_{-\infty}^{+\infty} n_e(y)\exp(-jky)dy \tag{4-12}$$

If the mechanical-electrical conversion characteristics of the transducer is included, Eq.(4-11) will be modified to

$$P_s(x',-l_0;k_0) = P(k_0)\frac{jA'k\delta\exp[j(k_0l_0-\pi/4)]}{2\sqrt{2\pi k_0}}\tilde{n}_e(-2k_0) \tag{4-13}$$

where $P(k)$ is the Fourier transform of the mechanical-electrical conversion characteristic function of the transducer; $P_s(x',-l_0;k_0)$ is the Fourier transform of the electrical signal produced by the rf echoes. The function $P(k)$ can be determined in the following way: a point scatterer is put at the focal point $(x',0)$ of the incident ultrasonic beam (in the case of a point scatterer, the object function $n_1(y)$ behaves as the δ-function), then the Fourier transform of the equivalent object function $n_e(y)$ can be expressed as

$$\tilde{n}_e(k) = \tilde{n}_e(-2k_0) = 1/\sqrt{l_0} \tag{4-14}$$

Finally, from Eq.(4-13), the mechanical-electrical conversion characteristics of the transducer can be obtained

$$P'(k_0) = \frac{2\sqrt{2\pi l_0}\exp[-j(k_0l_0+\pi/4)]}{k_0\sqrt{k_0}}P_{s\delta}(x',-l_0;k_0) \tag{4-15}$$

where $P_{s\delta}(x',-l_0;k_0)$ is the Fourier transform of the electrical signal produced by the point scatterer. $P'(k_0)$ is obtained from $P(k_0)$ by multiplying

the constant A'.

With Eq.(4-13), the relationship between the Fourier transform of the scattered rf echo signal and the Fourier transform of the equivalent object function on the line x = x' will be obtained

$$\tilde{n}_e(-2k_0) = \frac{2\sqrt{2\pi}\exp[-j(k_0 l_0+\pi/4)]}{k_0\sqrt{k_0}}\left[\frac{P_s(x',-l_0;k_0)}{P'(k_0)}\right] \qquad (4\text{-}16)$$

where P'(k) is determined by Eq.(4-15).

2. Spatial-Frequency Extrapolation and Image Reconstruction

As the incident wave used is a high-frequency bandpass signal with a certain bandwidth, from Eq.(4-16) only the high-frequency component of the equivalent object function $n_e(y)$ can be obtained. To reconstruct the equivalent object function using the known a priori knowledges, the Gerchberg-Papoulis (GP) frequency extrapolation technique[93] is used in this paper to recover the low-frequency component of the equivalent object function from the high-frequency component.

By the ordinary B-scan image, the outlines of the internal structures of the object can be determined, therefore, the rf echo signals returned from these outlines can be obtained and the phases of these rf echo signals can be identified. Fig.(4-2) (a) and Fig.(4-2)(b) are the waveforms of the rf echo signals returned from the water-agar and the agar-water interface respectively. It is noticed that their phases are different.

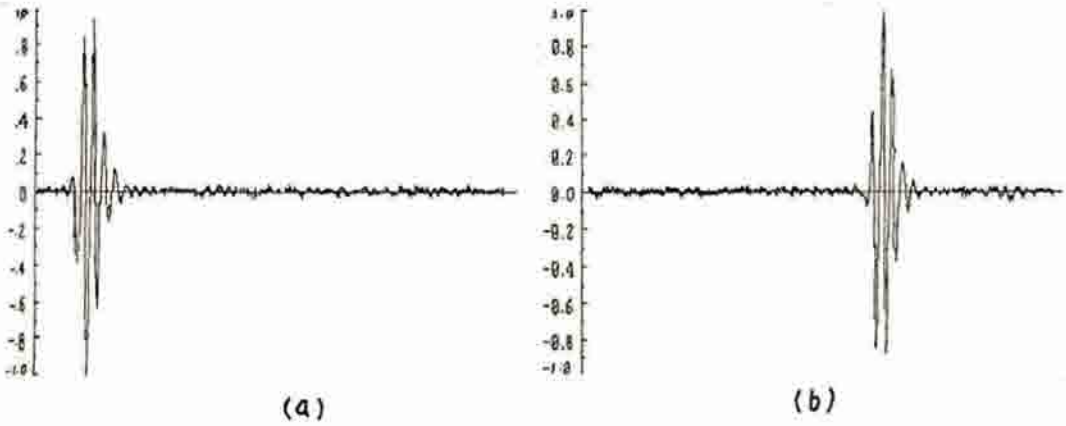

Fig.(4-2) (a) rf echo signals returned from the water—agar interface (b) from the agar—water interface

In order to utilize the phase information contained in the rf echo signals in the GP frequency extrapolation, it is required to derive the relationship between the Fourier transform of the derivative of the equivalent object function and the measured rf echo signals (the derivative of the equivalent object function can be obtained by simply multiplying the factor jk to its spatial frequency domain, here, k = -2k₀). Notating $n_e'(y)$ and $\tilde{n}_e'(k)$ as the derivative of the equivalent object function and its Fourier transform, from Eq.(4-16), one obtains

$$\tilde{n}_e'(-2k_0) = \frac{4\sqrt{2\pi}\exp[-j(k_0 l_0+3\pi/4)]}{\sqrt{k_0}}\left[\frac{P_s(x',-l_0;k_0)}{P'(k_0)}\right] \qquad (4\text{-}17)$$

The GP frequency extrapolation consists of seven steps (a) to (g) below.

It is an iteration procedure and is described briefly in the following

(a) Calculate $\tilde{n}_e'^{(1)}(k)$, the high-frequency component of $n_e'(y)$, using Eq.(4-17) ($\tilde{n}_e'^{(1)}(k)$ is used to replace the high-frequency component of each order partial reconstruction of the derivative of the equivalent object function in following iteration procedure).

(b) Find $n_e'^{(1)}(y)$, the first-order reconstruction of the derivative of the equivalent object function, by taking the IFFT of $\tilde{n}_e'^{(1)}(k)$.

---->(c) Determine the signs of $n_e'^{(1)}(y)$ on the outlines of the internal structures of the object in accordance with the phases of the rf echo signals returned from these outlines.

(d) Find $\tilde{n}_e'^{(2)}(k)$, the Fourier transform of the spatially modified $n_e'^{(1)}(y)$, by using the FFT. It is seen that the spectrum of $n_e'^{(1)}(y)$ is broadened and the low-frequency component comes out.

(e) Substituting $\tilde{n}_e'^{(1)}(k)$ into the high-frequency portion of $\tilde{n}_e'^{(2)}(k)$ and then taking the IFFT, we obtain $n_e'^{(2)}(y)$, the second-order partial reconstruction of the derivative of the equivalent object function.

----(f) Calculate the average of $|n_e'^{(2)}(y)-n_e'^{(1)}(y)|$ and see if it is smaller than a preset small positive value. If the condition is true, go to step (g), otherwise, go back to step (c).

(g) Obtain the equivalent object function $n_e(y)$ by integrating $n_e'^{(N)}(y)$, the Nth-order partial reconstruction of the derivative of the equivalent object function (the integration constant is determined by using the condition that $n_e(y) = 0$ if the point (x',y) is not in the object). By scanning the acoustical beam in a cross-section of the object, the equivalent object function $n_e(y)$ on different line $x = x'$ can be determined, and thus, tomographic image of the object can be reconstructed.

3. Description of Experimental System

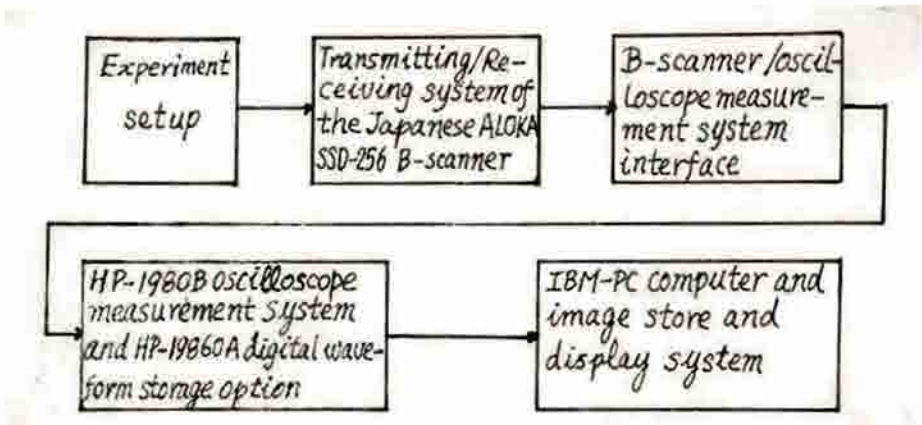

Block diagram of the experiment system

Fig.(4-3) is the block diagram of the experimental system. It consists of five parts: 1) experimental setup; 2) transmitting/receiving system of the Japanese ALOKA SSD-256 B-scanner[108]; 3) B-scanner/oscilloscope measurement system interface; 4) HP-1980B oscilloscope measurement system[109] and HP-

19860A digital waveform storage option[110]; and 5) IBM-PC computer and image store and display system. A brief description of each part of the experimental system will be given in the following.

Fig.(4-4) shows a draft of the water-tanker, the probe, the object to be imaged and the supporting framework of the probe and the object. The volume of the water tanker is 91 cm (long) x 68 cm (wide) x 70 cm (high), and the internal wall of the water-tanker is covered by ultrasound absorbing material. The object to be imaged is even in its long axial direction, i.e., the distribution of the acoustical parameters on each of its transversal cross-section is the same and the object can be looked as two-dimensional. The linear array probe is used to transmit the ultrasonic pulses and receive the echoes scattered from the object. Both the probe and the object are fixed on the supporting framework, forming probe-object system. The distance between the probe and the object is kept unchanged during the experiment, and the probe-object system is immersed in the water and is located in the center of the water-tanker. This system can be moved up and down to minimize the effects of the residual reflection signals coming from the wall and the bottom of the water-tanker in the measuring time window. The front view and the side view of the probe-object system are shown in Fig.(4-4) (a) and Fig.(4-4)(b) respectively.

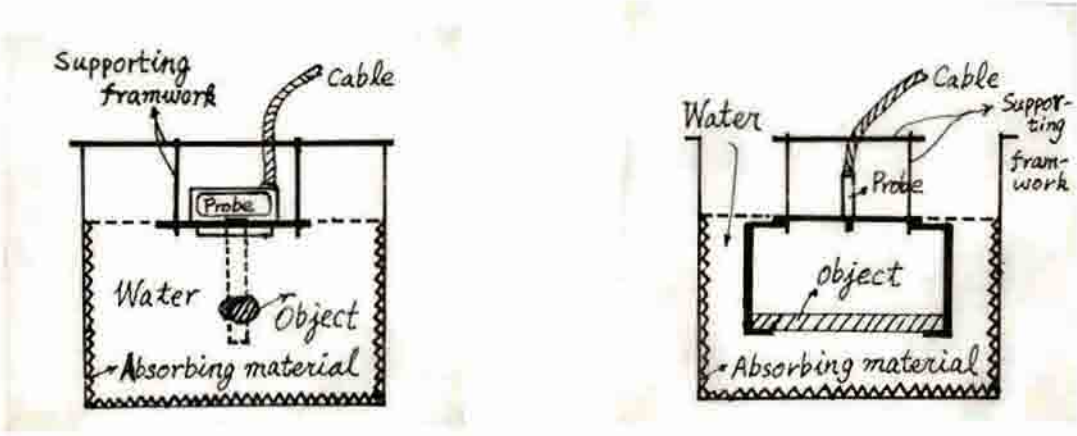

Fig.(4-4) (a) The front view and (b) the side view of the probe-object system

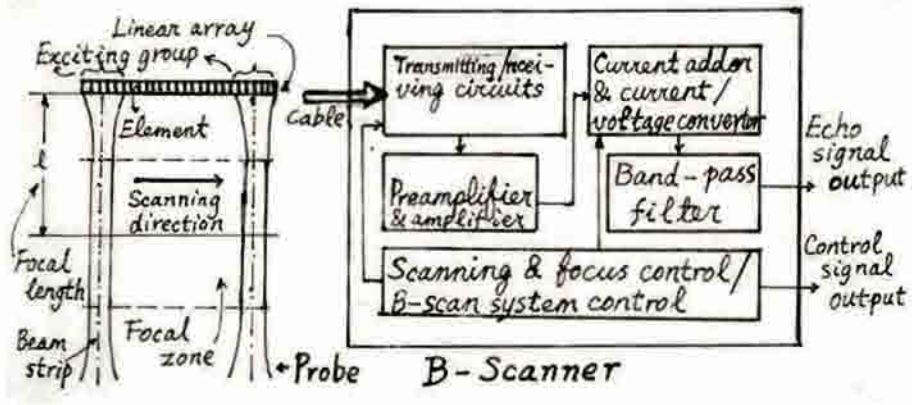

Fig.(4-5) Block diagram of the transmitting/receiving system of the Japanese ALOKA SSD-256 B-scanner

Fig.(4-5) is the transmitting/receiving system of the Japanese ALOKA SSD-256 B-scanner. The probe used in our experiments is the ALOKA UST-5024-3.5 linear array probe, it has 80 elements and its effective length is about 96 cm. To obtain the focused ultrasonic beam with a certain focal length, these

elements are not emitted individually, but emitted in groups and with different delay time for each element. After the emission, the group of elements convert to receivers and are focused electrically with the same focal length as that when they are used as the transmitters. The focused ultrasonic beam is scanned in the direction shown in Fig.(4-5) under the control of the electrical circuits. For every transmitting/receiving process, the rf echo signals are all filtered by a band-pass filter and then enter the full-wave detector, and the detected signals are fed into the DSC (digital scan convertor) for the transformation of the scanning format and for the image display. In the QRI method, the rf echo signals are connected out with high-frequency cable before detection, and are fed immediately to the datum acquisition system. Besides, the digital signals which controlled the transmission/reception of the ultrasonic pulses and the linear scan of the ultrasonic beam are connected out for the synchronization of the datum acquisition system and the B-scanner.

In our experimental system, the digital waveform storage oscilloscope is used for the datum acquisition of the rf echo signals. The HP-1980B oscilloscope measurement system when fitted with the HP-19860A digital waveform storage option will form the high-frequency digital waveform storage oscilloscope and allows the highest frequency of its input signal to be about 100 MHz. The digital waveform storage option can digitize the waveform of the analog signal displayed on the oscilloscope measurement system in 10-bit resolution and store them in its two digital memories. Each of the memories can hold as many as 501 samples and the samples can be transferred to computer by the standard IEEE-488 interface.

As HP-1980B is an oscilloscope, to display the waveform stably, it is necessary that the input signals are periodic. For sampling a periodic signals, low-sampling rate A/D convertor can be used to achieve high-sampling rate datum acquisition, which will lower the cost of the instrument greatly. Because of the use of the low-sampling rate A/D convertor, the datum acquisition time will be increased accordingly. As for the HP-1980B/HP-19860A digital waveform storage oscilloscope, only one sample can be acquired in every two periods of its input signals. Thereby, for a signal with a long period, the time for the datum acquisition will be very long. It is just the case in the datum acquisition of the rf echo signals of the B-scanner (the repeating rate of the rf echo signals of the B-scanner is about 37 ms, and the time for acquiring 501 samples will be about 37 s). therefore, to fulfil the datum acquisition in human body, it is necessary to develop a high-speed A/D system and a big datum buffer memory.

As the rf signals fed into the oscilloscope measurement system are filtered by the B-scanner, its highest frequency is confined to 5 MHz (the pass-band of the filter is extended from dozens of KHz to 5 MHz). If the bandwidth control knob of the oscilloscope measurement system is set to the band-limit position in the datum acquisition, the electrical noises which frequency is higher than 20 MHz will be excluded and hence the quality of the datum acquisition can be improved.

The interface circuit which connects the B-scanner and the oscilloscope measurement system is shown in Fig.(4-6). For the period of the rf echo signals in very long, it is difficult to display each part of the signals, especially those parts that have big time delay from the scan triggering signal. From the brief description of the digital waveform storage oscilloscope measurement system above, one can see that if the waveform displayed is unstable, the acquired data will be distorted severely (in fact, at 30MHz sampling rate, a delay with several hundreds of μs will cause serious distortion in the datum acquisition). In order to eliminate the random shift

of the displayed waveform along the time axis, an interface circuit which connects the B-scanner and the oscilloscope measurement system is developed and is mounted in the B-scanner. In Fig.(4-6), the US FRAME END signal indicates the end of each scanning, which means that all the echo information coming from the cross-section of the object has been obtained. The period of this signal is that of the rf echo signals of the B-scanner. In every period, the probe is transmitting and receiving 128 times, producing 128 ultrasonic beams. The US BLK signal indicates the beginning of each transmitting/receiving process, its period is about 270 μs which is the time that allows the reception of the echo signals coming from as deep as 18 cm of the biological soft tissues. The interface circuit consists of two parts: the first part generates a time window with a fixed width (it is about 18 μs which is two times of the pulse width of the US BLK signal); the second part is used to control the delay of the time window from the US FRAME END signal (the delay time is adjusted manually by a precision multi-circle voltmeter). When working, the time window is moved to the desired US BLK signal and the windowed US BLK signal is used to trigger the oscilloscope measurement system, which will fulfil the stable display and the stable datum acquisition of the rf echo signals returned from the object. Successively moving the time window, the rf echo signals in each transmitting/receiving procedure will be acquired and stored.

The data acquired by the digital waveform storage oscilloscope can then be transferred to the computer via the standard IEEE-488 interface under the control of the hardware and the software of the IBM-PC computer and will be saved in floppy disk after every 501 datum transfer is finished. (In order to make the IBM-PC computer have the hardware function of the standard IEEE-488 interface, a commercial multi-functional GPIB-PC board is inserted into a bus slot of the computer. Using software provided with the board, the high-level computer language can be used directly for the control of the functions of the digital waveform storage oscilloscope and its datum transfer to the computer). By the use of the data saved in the floppy disk and the software of the QRI method developed, images can be reconstructed. Finally, the reconstructed images are transferred to the ARLUNYA TF-4000 temporal filter and image store via the standard RS-232C interface with the control of the ARLUNYA computer transfer module (CTM), and are displayed on the high resolution JVC monitor.

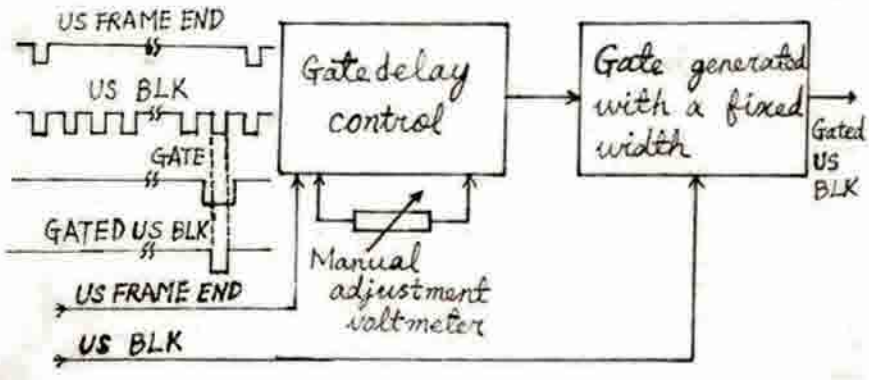

Fig.(4-6) The interface between the B-scanner and the oscilloscope measurement system

4. Experimental Results

(1) A computer simulation

Assume that the object function is a rectangular (see Fig.(4-7)), i.e.

$$n_1(y) = \begin{cases} A; & -152\Delta \leq y \leq 118\Delta \\ 0; & \text{otherwise} \end{cases} \qquad (4\text{-}18)$$

where Δ is the spatial stepping length of $n_1(y)$; A is a constant. Here, Δ = 0.0760 mm, A = 3.22. The number of the discretion points of $n_1(y)$ 1024.

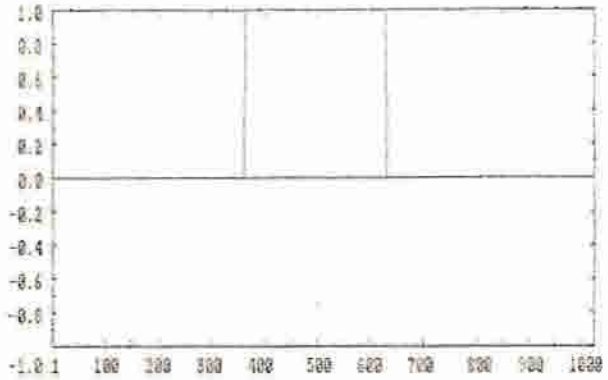

Fig.(4-7) The object function $n_1(y)$

From Eq.(4-10), the equivalent object function will be given by

$$n_e(y) = \begin{cases} A/\sqrt{l_0+y}; & -152\Delta \leq y \leq 118\Delta \\ 0 \quad ; & \text{otherwise} \end{cases} \qquad (4\text{-}19)$$

where L_0 = 115 mm. The figure of $n_e(y)$ is shown in Fig.(4-8), where its maximum value is $\max\{n_e(y)\}$ = 1.00. Next, we will assume that the high-frequency component of $n_e(y)$ has been obtained from the rf echo signals using Eq.(4-16). From this high-frequency component, the equivalent object function $n_e(y)$ and hence the object function $n_1(y)$ will be recovered by the GP frequency extrapolation technique.

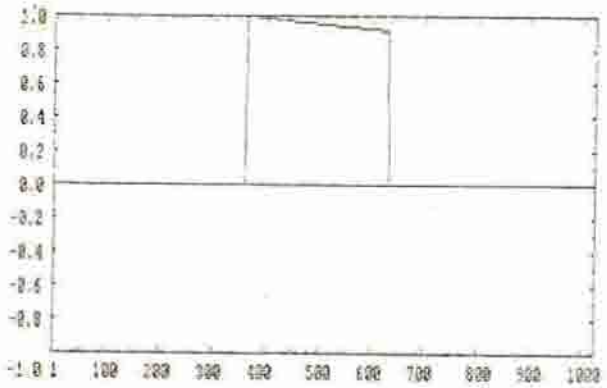

Fig.(4-8) The equivalent object function $n_e(y)$

Taking the FFT of $n_e(y)$, one will find the spectrum $\tilde{n}_e(k)$ (see Fig.(4-9)). Applying the Blackman window to $\tilde{n}_e(k)$, from Fig.(4-9) we obtain Fig.(4-10). Fig.(4-11) is obtained by taking the IFFT of the function in Fig.(4-10), and it represents the windowed equivalent object function and is an approximation of the equivalent object function determined by Eq.(4-19). It is seen that Fig.(4-11) is almost the same as Fig.(4-8), and the maximum value of the function in Fig.(4-11) is 0.999 which is also almost the same as that in

Fig.(4-8).

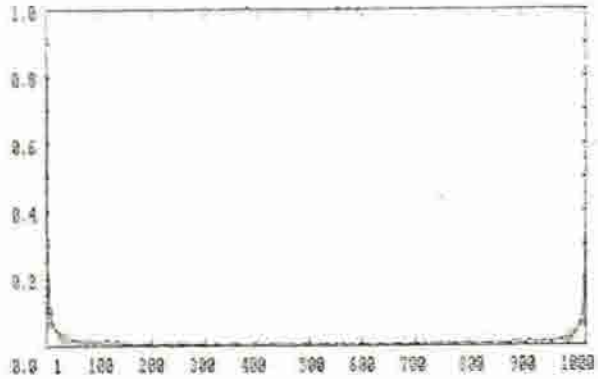

Fig.(4-9) $\tilde{n}_e(k)$, the spectrum of the equivalent object function $n_e(y)$

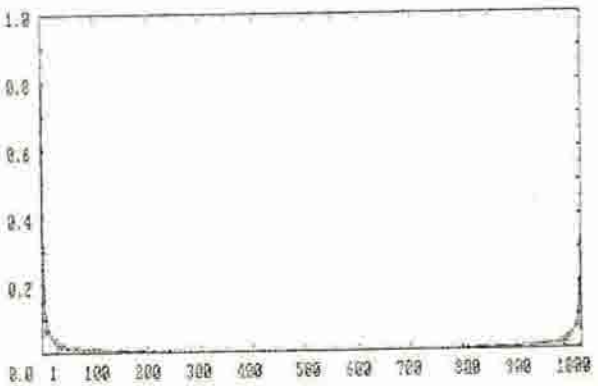

Fig.(4-10) The windowed spectrum of the equivalent object function $n_e(y)$

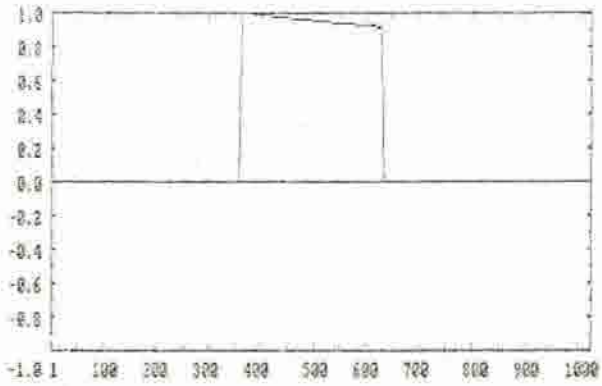

Fig.(4-11) The equivalent object function $n_e(y)$ whose spectrum is multiplied by the Blackman window

Differentiate the equivalent object function in Fig.(4-11), one obtains $n_e'(y)$, the derivative of the equivalent object function (to differentiate the equivalent object function is equal to multiply the factor jk to its Fourier domain) (see Fig.(4-12)). Fig.(4-13) shows $\tilde{n}_e'(k)$, the spectrum of $n_e'(y)$.

Excluding the low-frequency portion in Fig.(4-13), we have $\tilde{n}_e'^{(1)}(k)$, the high-frequency portion of $\tilde{n}_e'(k)$, which will be taken as the "correctly known" value in the following iterations of the GP frequency extrapolation (here, $\tilde{n}_e'^{(1)}(k)$ is assumed to be obtained from the Fourier transform of the measured rf echo

signals using Eq.(4-17)).

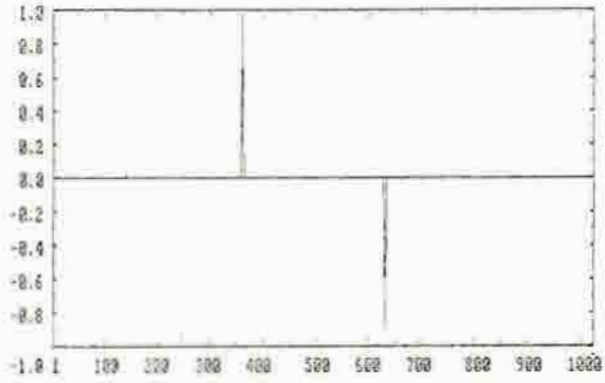

Fig.(4-12) $n_e'(y)$, the derivative of the equivalent object function $n_e(y)$ in Fig.(4-11)

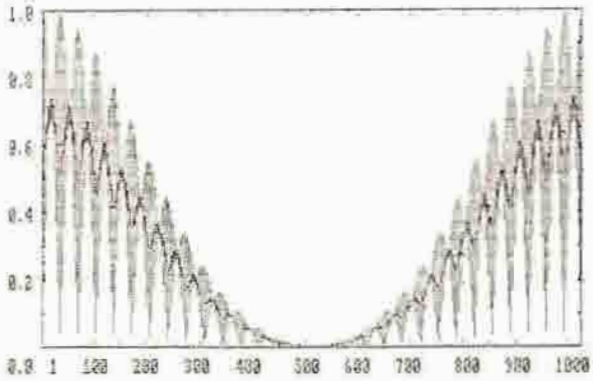

Fig.(4-13) $\tilde{n}_e'(k)$, the spectrum of $n_e'(y)$

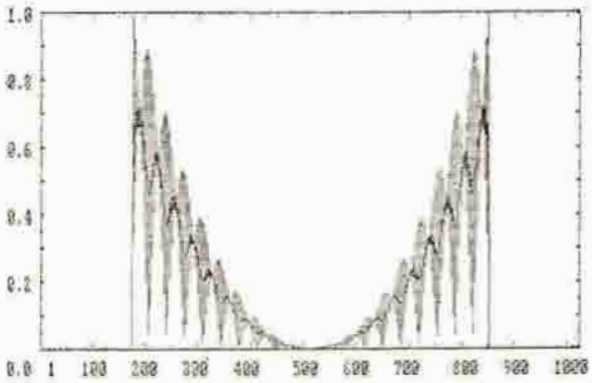

Fig.(4-14) $\tilde{n}_e'^{(1)}(k)$, the high-frequency portion of $\tilde{n}_e'(k)$

Taking the IFFT of $\tilde{n}_e'^{(1)}(k)$, $n_e'^{(1)}(y)$, the first-order partial reconstruction of the derivative of the equivalent object function will be obtained (see Fig.(4-15)).

It is seen that the outline position of $n_e(y)$ and the plus and the minus signs of $n_e'(y)$ on these outlines can be provided by Fig.(4-12). Modifying $n_e'^{(1)}(y)$ in the spatial domain using the outline and the phase information, then taking the FFT, $\tilde{n}_e'^{(2)}(k)$, the spectrum of the spatially modified $n_e'^{(1)}(y)$, can be found (see Fig.(4-16)). It can be observed from Fig.(4-16)

that the spectrum of $n_e'^{(1)}(y)$ has been broadened and the low-frequency component is emerged. Inserting the spectrum $\widetilde{n}_e'^{(1)}(k)$ into the high-frequency

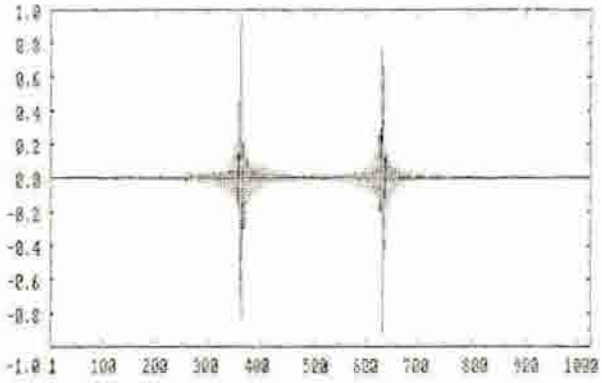

Fig.(4-15) $n_i'^{(1)}(y)$, the first-order partial reconstruction of the derivative of the equivalent object function

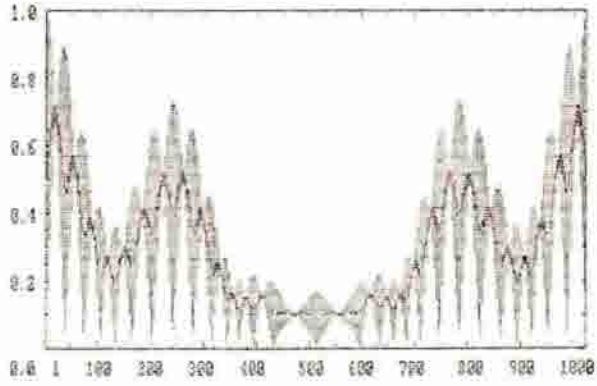

Fig.(4-16) $\widetilde{n}_e'^{(1)}(k)$, the spectrum of the spatially modified $n_i'^{(1)}(y)$

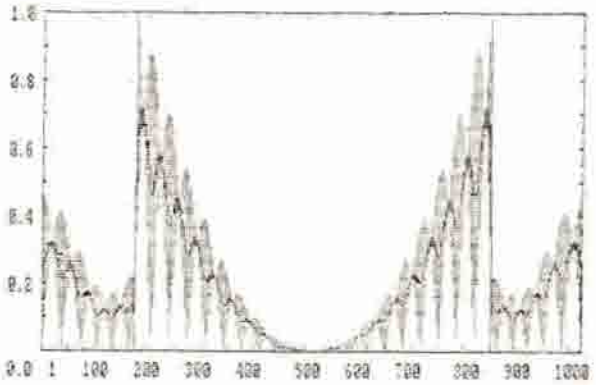

Fig.(4-17) High-frequency portion modified $\widetilde{n}_e'^{(1)}(k)$

portion of $\widetilde{n}_e'^{(2)}(k)$, one will get Fig.(4-17). Comparing Fig.(4-17) to Fig.(4-13), it is noticed that there is remarkable difference between them. Taking the IFFT of the frequency-domain modified spectrum, the second-order partial reconstruction of the derivative of the equivalent object function $n_e'^{(2)}(y)$ can be obtained. Repeating the iteration procedure above, $n_e'^{(30)}(y)$, the thirtieth-order partial reconstruction of the derivative of the equivalent object function, can be reconstructed. After the spatial-domain modifying, its spectrum is shown in Fig.(4-18). Comparing Fig.(4-18) to Fig.(4-13), it is

seen that there is little difference between them. Substituting $\tilde{n}_e'^{(1)}(k)$ into the high-frequency portion of Fig.(4-18), we obtain Fig.(4-19). Again, it is seen that there is little difference between these figures.

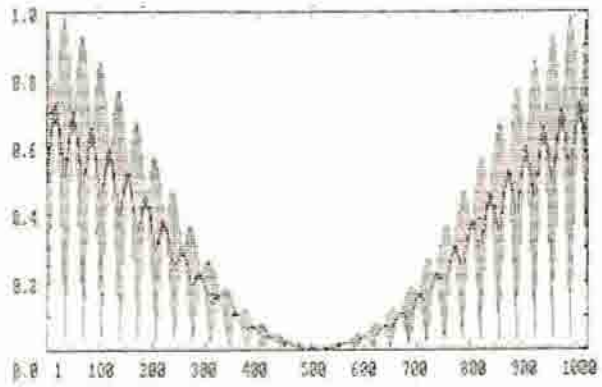

Fig.(4-18) The spectrum of the thirtieth-order partial reconstruction $n_1'^{(30)}(y)$ of the derivative of the equivalent object function

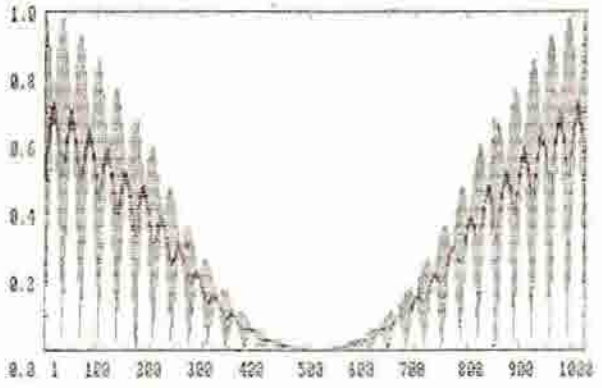

Fig.(4-19) The spectrum of the frequency-domain modified $n_1'^{(30)}(y)$

Taking the IFFT of the spectrum of the frequency-domain modified $n_e'^{(30)}(y)$ in Fig.(4-19) and then integrating the result with respect to y, one will obtain $n_e^{(31)}(y)$ (see Fig.(4-20)), the thirty-first-order partial reconstruction of the equivalent object function. The maximum value of $n_e^{(31)}(y)$ is about 0.905. From $n_e^{(31)}(y)$, one can obtain $n_1^{(31)}(y)$, the approximation of the object function $n_1(y)$ (see Fig.(4-21)). Fig.(4-21) and Fig.(4-20) are corresponding to Fig.(4-7) and Fig.(4-8), and are the results of the reconstructions of $n_1(y)$ and $n_e(y)$, respectively.

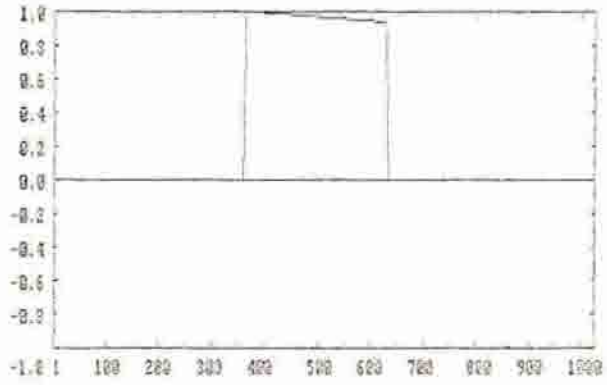

Fig.(4-20) $n_e^{(11)}(y)$, the approximation of the equivalent object function $n_e(y)$

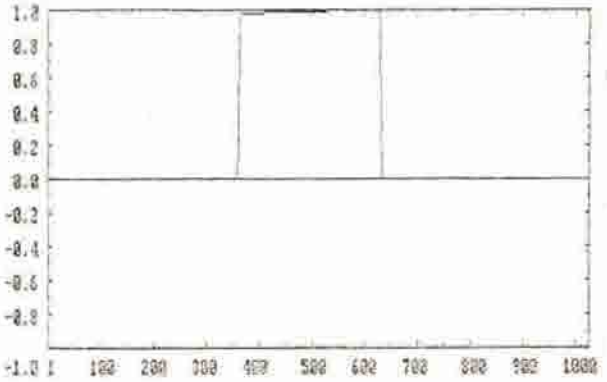

Fig.(4-21) $n_i^{(11)}(y)$, the approximation of the object function $n_i(y)$

From the computer simulation above, the equivalent object function $n_e(y)$, and hence the object function $n_i(y)$ can be reconstructed by the GP frequency extrapolation technique provided that the high-frequency component of $n_e(y)$ are correctly known and proper a priori knowledges are applied.

(2) Experimental results

In our experiments, agar is taken as the material for preparing the testing objects (phantoms). First, the agar powder is put into warmed water and is stirred by a grass rod to make it soaked. The stirring will be performed so gentle that little bubble is generated. After the agar-aqueous solution is compounded to a given volume percentage concentration, it is put into a high-pressure vessel for dissolving. Then, the dissolved agar-aqueous solution is poured into a mould prepared beforehand. After the solution is cooled down, it is fetched out and the phantom is formed. The mould used is a square channel and in the center of this channel, several grass rods which diameters are 2 mm and 3 mm are placed in a desired arrangement. The side length of the square channel is 20 mm and both the length of the square channel and the grass rods are 200 mm. As the phantoms are prepared evenly in its long axial direction, they can be looked as two-dimensional.

Fig.(4-22) are three phantoms prepared. The phantom in Fig.(4-22) (a) contains six small holes (one of them is of the diameter of 2 mm, others are of 3 mm) and is prepared from 4% agar-aqueous solution. The phantoms in Fig.(4-22)(b) and (c) have no holes in them and are prepared from 4% and 8% agar-aqueous solutions respectively. Fig.(4-23) (a), (b) and (c) are

photographs of the cross-section of the agar phantoms corresponding to Fig.(4-22) (a), (b) and (c), respectively.

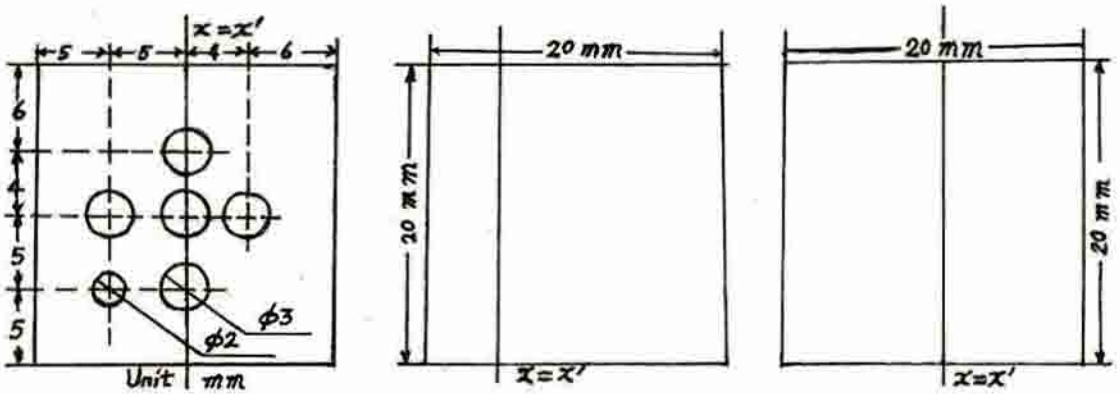

(a) (b) (c)

Fig.(4-22) (a) Phantom with six holes (made of 4% agar aqueous solution), (b) and (c) Phantoms with no holes (made of 4% and 8% agar aqueous solutions respectively)

(a) (b) (c)

Fig.(4-23) (a), (b) and (c) Photographs of the phantoms corresponding to Fig.(4-22) (a), (b) and (c) respectively

(a) (b) (c)

Fig.(4-24) (a), (b) and (c) are the images obtained by the ordinary B-scanner and are corresponding to Fig.(4-23) (a), (b) and (c) respectively

In order to determine the mechanical-electrical conversion characteristics, a thin thread of diameter of 0.04λ (the center frequency of the ultrasonic pulse used here is about 3 MHz and the wavelength of the pulse is about 0.5 mm) is taken as a two-dimensional point scatterer and it is placed at the focal point and on the center symmetric axis of the incident beam. Acquiring the rf echo signal returned from this point scatterer with the sampling rate of 30 MHz, from Eq.(4-15), the mechanical-electrical conversion

characteristics can be determined (for the highest frequency of the rf echo signal is about 5 MHz, the sampling rate used here satisfies the Nyquist sampling theorem. In what follows, 30 MHz sampling rate is adopted).

(a) (b) (c)

Fig.(4-25) (a), (b) and (c) are the images reconstructed by the QRI method and are corresponding to Fig.(4-23) (a), (b) and (c) respectively

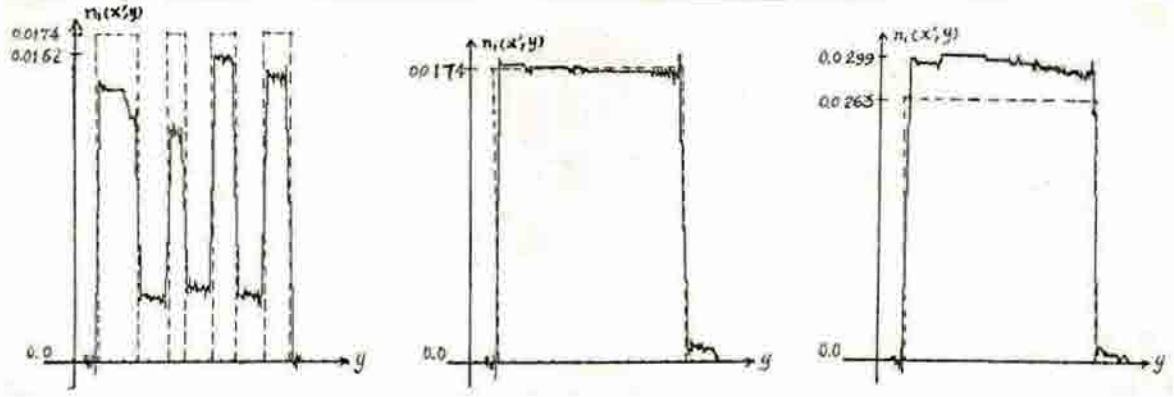

(a) (b) (c)

Fig.(4-26) (a), (b) and (c) are the figures of the comparisons of the reconstructed values (real lines) of the images in Fig.(4-25) (a), (b) and (c) and the real values (dashed lines) on the lines x = x' shown in Fig.(4-22) (a), (b) and (c) respectively

Fig.(4-24) (a), (b) and (c) are the B-scan images corresponding to Fig.(4-23) (a), (b) and (c) respectively. It can be seen from these figures that only the outline information is provided. Fig.(4-25) (a), (b) and (c) are the images reconstructed by the QRI method, and are corresponding to Fig.(4-23) (a), (b) and (c), respectively. Fig.(4-26) (a), (b) and (c) are the comparisons of the reconstructed values (real lines) and the real values (dashed lines) on the lines x = x' shown in Fig.(4-22) (a), (b) and (c), and are corresponding to Fig.(4-25) (a), (b) and (c), respectively. Here, the reconstructed values are only of relative meaning because there is a constant factor A' in Eq.(4-13) which is to be determined by the experiment, and the comparisons are relative to the average of the reconstructed values of Fig.(4-25) (b) on the line x = x' in Fig.(4-22) (b). It is noticed from Fig.(4-24), Fig.(4-25) and Fig.(4-26) that the images reconstructed by the QRI method are more helpful in understanding the internal structures of the testing objects than those obtained by the B-scanner, and to a certain extent, they are quantitative. Therefore, the QRI method is more liable to be used for tissue characterizations and will increase the ability of the B-scanner for diagnosing diseases.

V. SUMMARY

This paper gives a detailed theoretical analysis of the reconstruction algorithms of the diffraction tomography in the different datum acquisition geometries. As a result, the imaging quality and the image reconstruction speed of these algorithms are improved greatly. Although the great advances has been achieved in the study of the diffraction tomography, further researches should be carried out if the diffraction tomography is to be eventually used in clinic.

The QRI method proposed in this paper makes full use of the available transmitting/receiving system of the B-scanner and can provide the quantitative information of the distribution of the acoustical parameters of the biological soft tissues that the ordinary B-scanner can not provide. Therefore, it is hopeful that the QRI method is combined with the ordinary B-scanner to strengthen the ability of tissue characterizations and diagnosing diseases. In addition to the detailed theoretical derivation of the QRI method and the computer simulation, a full set of experimental system is designed and developed. With this experimental system, practical data from the testing objects are acquired and good images are reconstructed.

Although the QRI method reveals a good prospect of clinical applications, it is still far from being perfect. Several problems that are associated with the practical medical imaging, such as, the absorption of the ultrasonic wave in biological soft tissues, the scattering of the ultrasonic field by the unevenness of the distribution of the density of the biological soft tissues, the effect of the noises to the phase determination of the rf echo signals, should be considered. Besides, an AC LOG amplifier or time/gain convertor with small nonlinear distortion and big dynamic range should be developed to increase the resolution of the datum acquisition of the signals returned from the depth of the biological soft tissues; high-speed datum acquisition system and large-capacity buffer memory are required for the real-time datum acquisition of the signals returned from human body. In addition, because the agar phantoms used in the experiment are different from the biological soft tissues in some features, further theoretical and experimental studies should be carried out in the biological soft tissues.

ACKNOWLEDGEMENTS

The author gives his heartfelt thanks to the supervisor, Prof. and Dr.-Eng. Yu Wei, for her help in his pursuing Ph.D degree and writing the paper. Although she is the president of Southeast University and is very busy, she takes time for the concrete guiding of the work.

The author is also grateful to the teachers and the graduates in the Department of Biological Engineering for their help. The discussions with them are appreciated.

VI. REFERENCES

1. G.N. Hounsfield, "A Method and Apparatus for Examination of a Body by Radiation such as X or Gamma Radiation", Patent Specification 1283915, The Patent Office, London, England, 1972

2. G.N. Hounsfield, "Computerized transverse axial scanning tomography: Part I, description of the system, Br.J.Radiol., Vol.46, 1973, pp.1016-1022

3. A.H. Andersen and A.C. Kak, "Digital Ray Tracing in Two-Dimensional Refractive Fields", J.Acous.S.A., Vol.5, No.5, 1982

4. D. Blyth, G. Cavayne, M. Cleary, R. Fleming, T. Koch, L. Mears, J. McCaffrey and J. Whiting, "An Ultrasonic Computer-Assisted Tomographic Scanner", Australasian Phys. Sci. Med., Vol.2, Mar./Apr.1979, pp.141-153

5. G.H. Brandenburger, J.E. Klepper, J.R. Miller and D.L. Synder, "Effects of Anisotropy in the Ultrasonic Attenuation of Tissue on Computed Tomography", Ultrasonic Imaging, Vol.3, 1981, pp.113-147

6. P.L. Carson, T.V. Oughton and W.R. Hendee, "Ultrasound Transaxial Tomography by Reconstruction", Ultrasound in Medicine, Plenum Press, D.N. White and R.W. Barnes, eds., Vol.2, 1976, pp.391-400

7. P.L. Carson, D.R. Dick, C.A. Thieme, M.L. Dick, E.J. Hayly, T.V. Oughton, G.L. Dubuque and H.P. Hay, "Initial Investigation of Computed Tomography for Breast Imaging with Focused Ultrasound Beams", Ultrasound in Medicine, D.N. White and R.A. Lyons, eds., Plenum, New York, 1978, pp.319-322

8. C.R. Crawford and A.C. Kak, "Multipath Artifacts in Ultrasonic Transmission Tomography", Ultrasonic Imaging, 1982

9. K.A. Dines and A.C. Kak, "Ultrasonic Attenuation Tomography of Soft Biological Tissues", Ultrasonic Imaging, Vol.1, 1979, pp.16-33

10. N.H. Farhat and C.K. Chan, "Three-dimensional Imaging by Wave-Vector Diversity", Acoustical Holography, Vol.8, 1980, pp.499-516

11. G.H. Glover and J.L. Sharp, "Reconstruction of Ultrasound Propagation Speed Distribution in Soft Tissue: Time-of-Flight Tomography", IEEE Trans. Sonics & Ultrasonics, Vol.24, 1977, pp.229-234

12. J.F. Greenleaf, S.A. Johnson, S.L. Lee, G.T. Herman and E.H. Wood, "Algebraic Reconstruction of Spatial Distributions of Acoustic Absorption within Tissue from Their Two-Dimensional Acoustic Projections", Acoustical Holography, Plenum Press, New York, Vol.5, 1974, pp.591-603

13. J.F. Greenleaf, S.A. Johnson, W.F. Samayoa and F.A. Duck, "Algebraic Reconstruction of Spatial Distributions of Acoustic Velocities in Tissue from Their Time-of-Flight Profiles", Acoustical Holography, Plenum Press, New York, Vol.6, 1975, pp.71-90

14. J.F. Greenleaf, S.A. Johnson and A. Lent, "Measurement of Spatial Distribution of Refractive Index in Tissues by Ultrasonic Computer Assisted Tomography", Ultrasound Med. Biol., Vol.3, Oct.1978, pp.327-339

15. J.F. Greenleaf, S.K. Kenue, B. Rajagoplan, R.C. Bahn and S.A. Johnson, "Breast Imaging by Ultrasonic Computer-Assisted Tomography", Acoustical Imaging, A.F. Metherell, ed., Vol.8, 1980, pp.599-614

16. J.F. Greenleaf and R.C. Bahn, "Clinical Imaging with Transmissive Ultrasonic Computerized Tomography", IEEE Trans. Biomedical Engineering, Vol.28, No.2, Feb.1981, pp.177-185

17. J.F. Greenleaf, "Computerized Tomography with Ultrasound", Proc.IEEE, Vol.71, No.3, Mar.1983, pp.330-337

18. J.P. Havlice and J.C. Taenzer, "Medical Ultrasonic Imaging: An Overview of Principles and Instrumentation", Proc.IEEE, Vol.67, No.4, 1979

19. C.V. Jakowatz and A.C. Kak, "Computerized Tomography with X-Rays and Ultrasound", School of Elec. Eng., Purdue University, Resp. Rep. TR-EE 78-26, 1978

20. S.A Johnson, J.F. Greenleaf, W.A. Samayoa, F.A. Duck and J.D. Sjostrand, "Reconstruction of Three-Dimensional Velocity Fields and Other Parameters by Acoustical Ray Tracing", Proc. Ultrasonics Symposium, New York, 1975, pp.46-51

21. S.A. Johnson, M. Tanaka and E.C. Bahn, "High Resolution Ultrasound Echo and Reconstruction Imaging from Temporal and Spatial Projections by Adaptive Ray Tracing", International Conference on Pattern Recognition, IJCPR, 1978, pp.846-850

22. S.A. Johnson and J.F. Greenleaf, "New Ultrasound and Related Imaging Techniques", IEEE Trans. Nuclear Science, Vol.26, No.2, April 1979, pp.2812-2816

23. J.H. Kim, S.B. park and S.A. Johnson, "Tomographic Imaging of Ultrasonic Reflectivity with Correction for Acoustic Speed Variations", Ultrasonic Imaging, Vol.6, 1984, pp.304-312

24. S.J. Norton and M. Linzer, "Ultrasonic Reflectivity Tomography: Reconstruction with Circular Transducer Arrays", Ultrasonic Imaging, Vol.1, 1979, pp.154-184

25. S.J. Norton and M. Linzer, "Correcting for Ray Refraction in Velocity and Attenuation Tomography: A Perturbation Approach", Ultrasonic Imaging, Vol.4, 1982, pp.201-233

26. H. Schomberg, W. Beil, G.C. McKinnon, R. Proksa and O. Tschendel, "Tomographie a Ultrasons Assistee par Ordinateur", ACTA Electronica, Vol.26, No.1-2, 1984, pp.121-128

27. C.P. Schueler, B. Lee and G. Wade, "Fundamentals of Digital Ultrasonic Imaging", IEEE Trans. Sonics & Ultrasonics, Vol.31, No.4, Jul.1984, pp.195-217

28. F.J. Paoloni, "The Effects of Attenuation on the Born Reconstruction Procedure for Microwave Diffraction Tomography", IEEE Trans. Microwave Theory and Techniques, Vol.34, No.3, Mar.1986

29. C. Pichot, L. Jofre, G. Peronnet and J.C. Bolomey, "Active Microwave Imaging of Inhomogeneous Bodies", IEEE Trans. Antennas and Propagation, Vol.33, No.4, April 1985, pp.416-425

30. P.M. Forgues and M. Goldbery, "Medical Computed Tomography Using Microwaves", IEEE 1980 Frontiers of Engineering in Health Care.

31. P.S. Rao and E. Santosh, "Computed Tomography with Microwaves", Radiology 135: Jun.1980, pp.769-770

32. L. Axel, P.H. Arger, and R.A. Zimmerman, "Applications of Computerized Tomography to Diagnostic Radiology", Proc.IEEE, Vol.71, No.3, Mar.1983, pp.293-297

33. P. Bloch and J.K. Udupa, "Application of Computerized Tomography to Radiation Therapy and Surgical Planning", Proc. IEEE, Vol.71, No.3, March 1983, pp.351-355

34. D.P. Boyd and M.J. Lipton, "Cardiac Computerized Tomography", Proc.IEEE, Vol.71, No.3, Mar.1983, pp.298-307

35. R.A. Brooks and G.D. Chiro, "Principles of Computer Assisted Tomography (CAT) in Radiographic and Radioisotropic Imaging", Phys. Med. Biol., Vol.21, 1976, pp.689-732

36. G.T. Herman, "Introduction to the Foundations of X-Ray Computed Tomography", Computer Aided Tomography and Ultrasonics in Medicine, J. Raviv, J.F. Greenleaf and G.T. Herman, eds., Amsterdam, The Netherlands:

[illegible], 1971, pp. [illegible]

17. [illegible], "Image [illegible] from Projections", Academic Press, 1981.

18. [illegible], "Computerized Tomography with Cone, Vertex and Ultrasonic Sources", Proc.IEEE, Vol.67, No.9, [illegible], pp.1267-1277.

19. [illegible], [illegible] and M. Persoz, "Image Reconstruction from Projections I: General Theoretical Considerations", Optik, Vol. [illegible], 1978, pp.13-17.

20. [illegible], [illegible] and [illegible], "Image Reconstruction from Projections III: Modified Back-Projection Methods", Optik, Vol.50, No. [illegible], pp.95-103.

21. [illegible], "Digital Demodulation of Multidimensional Signals from Their Projections", [illegible], Vol.[illegible], 1971, pp.211-223.

22. [illegible], [illegible], [illegible], [illegible] and [illegible], "High-Speed Three-Dimensional Computed Tomography", Proc.IEEE, Vol.71, No.7, July 1983, pp.[illegible].

23. [illegible], "Introduction to Computer Aided Tomography", [illegible], [illegible], [illegible], pp.[illegible].

24. [illegible], "[illegible] Reconstruction [illegible]", [illegible], Vol.[illegible], pp.[illegible].

25. [illegible], "[illegible] Reconstruction [illegible]", [illegible], Vol.[illegible], pp.[illegible].

26. [illegible], "[illegible] Reconstruction [illegible]", [illegible], Vol.[illegible], pp.[illegible].

27. [illegible], "[illegible] Reconstruction [illegible]", [illegible], Vol.[illegible], pp.[illegible].

28. [illegible], "[illegible] Reconstruction [illegible]", [illegible], Vol.[illegible], pp.[illegible].

29. [illegible], "[illegible] Reconstruction [illegible]", [illegible], Vol.[illegible], pp.[illegible].

30. [illegible], "[illegible] Reconstruction [illegible]", [illegible], Vol.[illegible], pp.[illegible].

31. [illegible], "[illegible] Reconstruction [illegible]", [illegible], Vol.[illegible], pp.[illegible].

32. [illegible], "[illegible] Reconstruction [illegible]", [illegible], Vol.[illegible], pp.[illegible].

57. S. Kawata and O. Nalcioglu, "Constrained Iterative Reconstruction by the Conjugate Gradient Method", IEEE Trans. Medical Imaging, Vol.4, No.2, Jun.1985

58. W.W. Kim, M.J. Berggren, S.A. Johnson, P. Stenger and C.B. Wilcox, "Inverse Scattering Solutions to the Exact Riccati Wave Equations by Iterative Rytov Approximations and Integral Field Calculations", Proc. Ultrasonics Symposium, 1985, pp.898-902

59. M. L. Tracy and S. A. Johnson, "Inverse Scattering Solutions by a Sinc Basis, Multiple Source, Moment Method -- Part II: Numerical Evaluations", Ultrasonic Imaging, Vol.5, 1983, pp.376-392

60. M. Slaney and A. C. Kak, "Imaging with Higher Order Diffraction Tomography", Proc. Ultrasonics Symposium, 1985, pp.808-813

61. M. Anini and A.C. Kak, "Distortion in Diffraction Tomography Caused by Multiple Scattering", IEEE Trans. Medical Imaging, Vol.2, No.4, Dec.1983, pp.176-185

62. M. Anini and A.C. Kak, "Multiple Scattering and Attenuation Phenomena in Diffraction Imaging", Technical Report, TR-EE-85-4, Purdue University, School of Electrical Engineering, 1985

63. R.H.T. Bates, R.A. Minard, "Compensation for Multiple Reflection", IEEE Trans. Sonics & Ultrasonics, Vol.31, No.4, Jul.1984, pp.330-336

64. G. Beylkin, "The Fundamental Identity for Iterated Spherical Means and the Inversion Formula for Diffraction Tomography and Inverse Scattering", J.Math.Phys., Vol.24, No.6, Jun.1983, pp.1399-1400

65. G. Beylkin and M.L. Oristaglio, "Distorted-Wave Born and Distorted-Wave Rytov Approximations", Optics Communications, Vol.53, No.4, March 15, 1985, pp.213-216

66. R. Dandliker and K. Weiss, "Reconstruction of the Three-Dimensional Refractive Index from Scattered Wave", Optics Communications, Vol.1, No.7, 1970, pp.323-328

67. A.J. Devaney, "A Filtered Backpropagation Algorithm for Diffraction Tomography", Ultrasonic Imaging, Vol.4, 1982, pp.336-350

68. A.J. Devaney, "A Computer Simulation Study of Diffraction Tomography", IEEE Trans. on Biomedical Engineering, Vol.BME-30, No.7, Jul.1983, pp.377-386

69. A.J. Devaney and G. Beylkin, "Diffraction Tomography Using Arbitrary Transmitter and Receiver Surface", Ultrasonic imaging, Vol. 6, 1984, pp.181-193

70. A.J. Devaney, "Ultrasound Tomography", Physics News in 1983 -- Medical and Biological Physics, Physics Today, Vol.37, No.1, Jan.1984, pp.s.37-s.38

71. A.J. Devaney, "Generalized Projection-Slice Theorem for Fan Beam Diffraction Tomography", Ultrasonic Imaging, Vol.7, 1985, pp.264-275

72. A.J. Devaney, "Variable Density Acoustic Tomography", J.Acoust.Soc.Am., Vol.78, No.1, Jul.1985, pp.120-130

73. J.L. Harris, "Diffraction and Resolving Power", J.Opt.S.A., Vol.54, 1964, pp.931-936

74. D. Miller and R. Ermert, "System Analysis of Ultrasound Reflection Mode Computerized Tomography", IEEE Trans. Sonics & Ultrasonics, Vol.31, No.4, Jul.1984, pp.240-250

75. M. Kaveh, R. K. Mueller and R. D. Iverson, "Ultrasonic Tomography Based on Perturbation Solutions of the Wave Equation", Computer Graphics and Image Processing, Vol.9, 1979, pp.105-116

76. M. Kaveh, R.K. Mueller, R. Rylander, T.B. Coulter and M. Soumekh, "Experimental Results in Ultrasonic

[illegible] Tomography," Proceedings, [illegible], pp. [illegible]

[illegible] W. [illegible], M. [illegible], and [illegible], "Diffraction Tomography of Some Optical Properties of Biological Cells," Proceedings, [illegible], [illegible], 1981.

[illegible] M. [illegible], M. [illegible], and [illegible], "Effects of Refraction in Diffraction Tomography Using Acoustic and Optical Beams," Proceedings, [illegible], [illegible], New York, [illegible], 1985.

[illegible] M. [illegible], M. [illegible], and [illegible], "Algebraic Reconstruction for Diffraction Tomography," IEEE Trans. Acoustics, Speech, and Signal Processing, [illegible], Vol. [illegible], pp. [illegible]

[illegible] [illegible], and [illegible], Statistical Angle-Multi-Frequency Diffraction Tomography," IEEE Trans. Acoustics, Speech, and Signal Processing, Vol. [illegible], pp. [illegible]

[illegible] [illegible], [illegible], and [illegible], "Limited Angle Diffraction Tomography and Its Application to Planar Scanning Systems," IEEE Trans. Acoustics, Speech, and Signal Processing, [illegible], [illegible], 1985.

[illegible] [illegible], [illegible], and [illegible], "[illegible] Diffraction Tomography," [illegible], [illegible], pp. [illegible]

[illegible] [illegible], "[illegible] Diffraction Tomography," [illegible], [illegible], [illegible], pp. [illegible]

[illegible] [illegible], "[illegible] Algorithms for Synthetic Aperture Diffraction Tomography," [illegible], [illegible], [illegible], pp. [illegible]

[illegible] [illegible], [illegible], and [illegible], "Diffraction Tomography and Applications in Ultrasonic Imaging," [illegible], Vol. [illegible], [illegible], 1983, pp. [illegible]

[illegible] [illegible], "Diffraction Tomography in the Near-Field," [illegible], Vol. [illegible], 1981, pp. [illegible]

[illegible] [illegible], "Diffraction Tomography," [illegible], Vol. [illegible], 1985.

[illegible] [illegible], [illegible], and [illegible], "Limited Diffraction Tomography for Ultrasonic Imaging," [illegible], [illegible], [illegible], pp. [illegible]

[illegible] [illegible], [illegible], and [illegible], "Synthetic Aperture Diffraction Tomography and Its Interpretation from the Geophysical," IEEE Trans. [illegible] and Ultrasonics, Vol. [illegible], No. [illegible], Jul. 1984, pp. [illegible]

[illegible] [illegible], "[illegible] Applications of [illegible] Tomography," [illegible], [illegible], pp. [illegible]

[illegible] [illegible], [illegible], and [illegible], "[illegible] Algorithms for Diffraction Tomography Using Limited Aperture Data," IEEE Trans. on Acoustics, Speech, Signal Processing, [illegible], pp. [illegible]

[illegible] [illegible], [illegible], and [illegible], "High Diffraction Tomography Applied to the Inverse [illegible] Problem Part I: Continuous Waves," [illegible], Vol. [illegible], pp. [illegible]

[illegible] [illegible], [illegible], and [illegible], "[illegible] Diffraction Tomography," [illegible], Vol. [illegible], pp. [illegible]

[illegible] [illegible], [illegible], and [illegible], "Effect of Imaging with Plane-Wave Diffraction Tomography," IEEE Trans. [illegible] and Ultrasonics, Vol. [illegible], No. [illegible], pp. [illegible]

[illegible] [illegible], [illegible], "Image Reconstruction from Frequency Domain Data on [illegible] Surfaces," [illegible], Vol. [illegible], pp. [illegible]

96. M. Soumekh, M. Kaveh, "A Theoretical Study of Model Approximation Errors in Diffraction Tomography", IEEE Trans. Ultrason. Ferroelec. Freq. Control, Vol.33, No.1, Jan.1986, pp.10-20

97. M. Soumekh, "An Improvement to the Rytov Approximation in Diffraction Tomography", IEEE Trans. Ultrason. Ferroelec. Freq. Control, Vol.33, No.4, Jul.1986, pp.394-401

98. D.J. Vezzetti, and S.Q. Aks, "Reconstruction from Scattering data: Analysis and Improvements of the Inverse Born Approximation", Ultrasonic Imaging, Vol.1, No.4, 1980, pp.333-345

99. H. L. Yue and Y. Wei, "A Fast Reconstruction Algorithm for Diffraction Tomography", 16th International Symposium on Acoustical Imaging, Chicago, June 10-12, 1987

100. M. Zhang, Z. M. Cai and Y. Wei, "A New Reconstruction Algorithm for Diffraction Tomography", International Radio Conference, Budapest, 1986

101. P.M. Morse, H. Feshbach, "Methods of Theoretical Physics", McGraw-Hill, New York, 1953, Ch.2, 5, 7 & 11

102. P.M. Morse, K.V. Ingard, "Theoretical Acoustics", McGraw-Hill, New York, 1968, Chap.8

103. A. Ishimaru, "Wave Propagation and Scattering in Random Media", Vol.2, Ch.17, Academic Press, 1978

104. K. E. Atkinson, "An Introduction to Numerical Analysis", John Wiley & Sons, New York, 1978

105. Q.Y. Li, N.C. Wang and D.Y. Yi, "Numerical Analysis", Huazhong Institute of Technology, July 1982 (In Chinese)

106. A.V. Oppenheim and R.W. Schafer, "Digital Signal Processing", Prentice-Hall, Inc., Englewood Cliffs, New Jersey, Ch.5, 1975

107. J.W. Goodman, "Introduction to Fourier Optics", McGraw-Hill, New York, 1968, Chap. 3

108. ALOKA Co. Ltd., Japan, "SSD-256 Training Manual".

109. HP Co. Ltd., America, "HP-1980A/B Oscilloscope Measurement System -- Operating Manual".

110. HP Co. Ltd., America, "HP-1986A Digital Waveform Storage Option -- Operating Manual".

PUBLICATIONS OF THE AUTHOR DURING THE PERIOD OF BEING A GRADUATE STUDENT FOR Ph.D DEGREE

A1. Jian-Yu Lu and Yu Wei, "Cubic Spline Interpolation and Its Application to Diffraction Tomography", on the 2nd National Youth Conference of Biomedical Engineering (Nanjing, China, November 17-21, 1987).

A2. Jian-Yu Lu and Yu Wei, "Transmission-Reflection Diffraction Tomography and Its Computer Implementations", on the 2nd National Youth Conference of Biomedical Engineering (Nanjing, China, November 17-21, 1987).

A3. Jian-Yu Lu, "A Computational Study for Synthetic Aperture Diffraction Tomography: Interpolation versus Interpolation-Free", in Acoustical Imaging, Vol.16, Edited by Dr. Lawrence W. Kessler, 1987 (16th International Symposium on Acoustical Imaging, Chicago, America, June 10-12, 1987)

A4. Jian-Yu Lu, "A Study of the Fourier-Domain Interpolation Reconstruction Algorithms for Synthetic Aperture Diffraction Tomography", Proceedings of the China-Japan Joint Conference on Ultrasonics (Nanjing, China, May 11-14, 1987), pp.395-399

A5. Jian-Yu Lu and Yu Wei, "An Improvement of the Fourier-Domain Interpolation Reconstruction Algorithms for Synthetic Aperture Diffraction Tomography", on the 2nd National Youth Conference of Biomedical Engineering (Nanjing, China, November 17-21, 1987). To be published in Applied Acoustics (a Chinese Quarterly), No.1, Jan.1989

A6. Jian-Yu Lu and Yu Wei, "A New Method for Quantitative Reflection Imaging", in Acoustical Imaging, Vol.17, Edited by Dr. Jun-ichi Kushibiki, 1988 (17th International Symposium on Acoustical Imaging, Sendai, Japan, May 31-June 2, 1988)

A7. Jian-Yu Lu and Yu Wei, "Experiments for a New Quantitative Reflection Imaging Method", (World Congress on Medical Physics and Biomedical Engineering, August 6-12, 1988, U. S. A.)

A8. Jian-Yu Lu, "Computerized Tomography", (invited paper), on the 1st National Graduate-Student Conference of Communication Theory and Technology (Nanjing, China, December 6-7, 1986). It has been included in the Conference Proceedings.

Aperil 30, 1988